

A 95 GHz Class I Methanol Maser Survey Toward A Sample of GLIMPSE Point Sources Associated with BGPS Clumps

Xi Chen^{1,2}, Simon P. Ellingsen³, Jin-Hua He⁴, Ye Xu⁵, Cong-Gui Gan^{1,2}, Zhi-Qiang Shen^{1,2}, Tao An^{1,2}, Yan Sun⁵, Bing-Gang Ju⁵

ABSTRACT

We report a survey with the Purple Mountain Observatory (PMO) 13.7-m radio telescope for class I methanol masers from the 95 GHz ($8_0 - 7_1A^+$) transition. The 214 target sources were selected by combining information from both the *Spitzer* GLIMPSE and 1.1 mm BGPS survey catalogs. The observed sources satisfy both the GLIMPSE mid-IR criteria of $[3.6]-[4.5]>1.3$, $[3.6]-[5.8]>2.5$, $[3.6]-[8.0]>2.5$ and 8.0 μm magnitude less than 10, and also have an associated 1.1 mm BGPS source. Class I methanol maser emission was detected in 63 sources, corresponding to a detection rate of 29% for this survey. For the majority of detections (43), this is the first identification of a class I methanol maser associated with these sources. We show that the intensity of the class I methanol maser emission is not closely related to mid-IR intensity or the colors of the GLIMPSE point sources, however, it is closely correlated with properties (mass and beam-averaged column density) of the BGPS sources. Comparison of measures of star formation activity for the BGPS sources with and without class I methanol masers indicate that the sources with class I methanol masers usually have higher column density and larger flux density than those without them. Our results predict that the criteria $\log(S_{int}) \leq -38.0 + 1.72\log(N_{H_2}^{beam})$ and $\log(N_{H_2}^{beam}) \geq 22.1$, which utilizes both the integrated flux density (S_{int}) and beam-averaged column density ($N_{H_2}^{beam}$) of the BGPS sources, are very efficient for selecting sources likely to have an associated class I methanol maser. Our expectation is that searches

¹Key Laboratory for Research in Galaxies and Cosmology, Shanghai Astronomical Observatory, Chinese Academy of Sciences, Shanghai 200030, China; chenxi@shao.ac.cn

²Key Laboratory of Radio Astronomy, Chinese Academy of Sciences, China

³School of Mathematics and Physics, University of Tasmania, Hobart, Tasmania, Australia

⁴National Astronomical Observatories/Yunnan Observatory, Chinese Academy of Sciences, Kunming 650011, China

⁵Purple Mountain Observatory, Chinese Academy of Sciences, Nanjing 210008, China

using these criteria will detect 90% of the predicted number of class I methanol masers from the full BGPS catalog (~ 1000), and do so with a high detection efficiency ($\sim 75\%$).

Subject headings: masers – stars:formation – ISM: molecules – radio lines: ISM
– infrared: ISM

1. Introduction

Methanol masers from a number of transitions are common in active star forming regions (SFRs) and have been empirically classified into two categories (class I and class II). Initial studies found that strong emission from the two classes are preferentially found towards different star formation regions (Batra et al. 1988; Menten 1991). Class I methanol masers (e.g. the $7_0 - 6_1 A^+$ and $8_0 - 7_1 A^+$ at 44 and 95 GHz respectively) are typically observed in multiple locations across the star-forming region spread over an area up to a parsec in extent (e.g. Plambeck & Menten 1990; Kurtz et al. 2004; Voronkov et al. 2006; Cyganowski et al. 2009). In contrast class II methanol masers (e.g. the $5_1 - 6_0 A^+$ and $2_0 - 3_{-1} E$ at 6.7 and 12.2 GHz respectively) are often associated with ultracompact (UC) HII regions, infrared sources and OH masers and reside close to (within $1''$) a high-mass young stellar objects (YSO) (e.g., Caswell et al. 2010). See Müller et al. (2004) for accurate rest frequencies and other basic data on methanol maser transitions. The empirical classification and observational findings were supported by early theoretical models of methanol masers which suggest that the pumping mechanism of class I masers is dominated by collisions with molecular hydrogen, in contrast to class II masers which are pumped by external far-infrared radiation (Cragg et al. 1992). More recent modelling has found that in some cases weak class II methanol masers can be associated with strong class I masers and vice versa (e.g. Voronkov et al. 2005), i.e., bright masers of different classes can not reside in the same volume of gas. High spatial resolution observations (e.g. Cyganowski et al. 2009) suggest that where both masers are seen in the same vicinity, while the two types of masers are not co-spatial on arcsecond scales, they are often driven by the same young stellar object.

A number of surveys have been performed for class II methanol masers especially at 6.7 GHz, resulting in the detection of ~ 900 class II maser sources in the Galaxy to date (e.g., the surveys summarized in the compilation of Pestalozzi et al. 2005 and the recent searches of Ellingsen 2007, Pandian et al. 2007, Xu et al. 2008, 2009, Green et al. 2009, 2010, 2012 and Caswell et al. 2010, 2011). Class I methanol masers are less well studied than class II masers, but have recently become the focus of more intense research (e.g., Sarma & Momjian 2009, 2011; Fontani et al. 2010; Kalenskii et al. 2010; Voronkov et al. 2010a, b,

2011; Chambers et al. 2011; Chen et al. 2011; Fish et al. 2011; Pihlström et al. 2011). Early studies of class I masers include only a small number of large surveys (mainly at 44 and 95 GHz), primarily undertaken with single-dish telescopes (e.g. Haschick et al. 1990; Slysh et al. 1994; Val’tts et al. 2000; Ellingsen 2005) along with a few smaller scale interferometric searches (e.g. Kurtz et al 2004, Cyganowski et al. 2009). Recently, some surveys have been done at other transitions of class I methanol, e.g. 9.9 GHz by Voronkov et al. (2010a) and a new class I methanol maser transition at 23.4 GHz has been discovered by Voronkov et al. (2011). Interferometric observations show that the class I methanol masers at different transitions (e.g., 36 GHz and 44 GHz) usually have similar larger-scale spatial distributions, but are rarely found to produce a maser at the same site (e.g., Fish et al. 2011). Surveys have revealed that class I methanol maser (unlike class II masers) are associated not only with high-mass star formation, but also lower mass counterparts (Kalenskii et al. 2010).

Recently Chen et al. (2009) demonstrated that a new sample of massive young stellar object (MYSO) candidates associated with ongoing outflows (known as extended green objects or EGOs and identified from the *Spitzer* GLIMPSE survey by Cyganowski et al. (2008)), provide another productive target for class I maser searches. On the basis of their statistical analysis Chen et al. predicted a detection rate of 67% for class I masers toward EGOs. A follow-up systemic survey towards a complete EGO sample (192 sources) with the Australia Telescope National Facility (ATNF) Mopra 22-m radio telescope resulted in the detection of 105 new 95 GHz class I methanol masers (Chen et al. 2011). The majority of these detections (92) are newly-identified class I methanol maser sources, thus demonstrating that there is a high detection rate (55%) of class I methanol masers toward EGOs. This search, combined with previous observations increased the number of known class I methanol masers to ~ 300 . Chambers et al. (2011) obtained an apparently contradictory result for a similar search, achieving a relatively low detection rate ($8/31=26\%$) of class I methanol maser at 44 GHz towards $4.5 \mu\text{m}$ emission sources. The low detection rate in this survey may be because Chambers et al. have targeted sources with relatively less extended green emission than the EGOs identified by Cyganowski et al. (2008).

The generally held view of class I methanol masers is that they trace regions of mildly shocked gas, where the methanol abundance is significantly enhanced and the gas is heated and compressed providing more frequent collisions. Voronkov et al. (2010a) suggested that the shocks which produce class I methanol masers may be driven into molecular clouds not only by outflows (it is worth noting that a high-velocity feature from a class I methanol maser associated with outflow parallel to the line of sight has been detected in the EGO source G309.38-0.13 by Voronkov et al. 2010b), but also from expanding HII regions. Based on the results of their analysis of GLIMPSE properties and the findings of Voronkov et al., Chen et al. (2011) suggest that class I methanol masers may arise at two distinct two-evolutionary

phases during the high-mass star formation process: they may appear as one of the first signatures of massive star formation associated with young outflows, and also that they can be re-activated at a later evolutionary stage associated with OH masers and HII regions.

Further searches for class I methanol masers are very important for our understanding of the range of environments and circumstances in which they arise. Ellingsen (2006) developed criteria for targeting class II methanol maser searches using GLIMPSE point source colors. He suggested that targeted searches toward GLIMPSE point sources with $[3.6]-[4.5] > 1.3$ and an $8.0 \mu\text{m}$ magnitude less than 10 will detect more than 80% of all class II methanol maser sources with an efficiency of greater than 10% (although the actual efficiency obtained from the only follow-up search reported to date is much lower (Ellingsen 2007)). In comparison, the mid-IR color analysis of GLIMPSE point sources toward EGOs undertaken by Chen et al. (2011) shows that the color-color region occupied by the GLIMPSE point sources towards EGOs which are, and are not, associated with class I methanol masers are very similar, and mostly located within color ranges $-0.6 < [5.8]-[8.0] < 1.4$ and $0.5 < [3.6]-[4.5] < 4.0$. This suggests that the GLIMPSE point source colors may not be a very sensitive diagnostic for constructing a sample to search for class I methanol masers. Despite the significant overlap in the color space occupied by EGOs with and without an associated class I methanol, Chen et al. (2011) do find the detection rate of class I methanol masers is higher in those sources with redder GLIMPSE point source colors. Therefore the reddest GLIMPSE point sources may provide a reasonable sample for searching for class I methanol masers with a relatively high detection efficiency. One point to note is that the implication of a relatively high detection efficiency for class I methanol masers for the redder GLIMPSE point sources is based on the EGO sample. The GLIMPSE point sources associated with EGOs are believed to be MYSOs with ongoing outflows, and the EGOs themselves have a high detection rate of class I methanol masers. Therefore a relatively high detection efficiency of class I methanol masers is not unexpected in these redder GLIMPSE point sources associated with EGOs. Further searches for class I methanol masers toward non-EGO associated GLIMPSE point sources is necessary to more reliably characterise the mid-IR characteristics of class I methanol maser sources. The mid-IR colors of some other astrophysical objects, (e.g. AGB stars) also are located within a similar color-color region as that found for class I methanol masers (Robitaille et al. 2008). Thus finding additional measures by which GLIMPSE point sources associated with active star formation can be distinguished from other objects with similar mid-IR colors is an important step required for such searches.

Recently the Bolocam Galactic Plane Survey (BGPS) has detected 1.1 mm thermal dust emission from thousands of regions of dense gas, many of which are closely associated with star formation. The typical H_2 column density of BGPS sources is $\sim 10^{22} \text{ cm}^{-2}$, the typical mass a few hundred M_\odot , and the typical size a parsec (Aguirre et al. 2011; Dunham et al.

2011a, b). So the BGPS is identifying high column density regions and is a sensitive tracer of massive clumps, in contrast to signposts such as class II methanol maser emission, which are only present once a YSO has formed. Dunham et al. (2011a) found that approximately half the BGPS sources contain at least one GLIMPSE source (within the area where both BGPS and GLIMPSE surveys overlap). Chen et al. (2011) found that the detection rate of class I methanol masers is significantly higher towards those EGOs with an associated BGPS source (35/54=65%) than for those without (1/9=11%), or in the complete EGO sample (55%). Dunham et al. (2011a) also found that EGOs are frequently associated with BGPS sources. Of the 84 EGOs within the BGPS survey area, 79 are associated with BGPS sources. All of the above factors suggest that the BGPS may be a useful supplement to the GLIMPSE point source catalog in constructing a reliable and efficient targeted sample for class I methanol masers.

In this paper, we report the results of a 95 GHz class I methanol maser survey towards a sample of GLIMPSE point sources with associated 1.1 mm BGPS sources which has been undertaken with the Purple Mountain Observatory (PMO) 13.7 m radio telescope. In Section 2 we describe the sample and observations, in Section 3 we present the results of the survey, analysis and discussion is given in Section 4, followed by a summary of the important results in Section 5.

2. Source selection and Observations

2.1. Source selection

We used the released catalogs from the GLIMPSE survey (version 2.0) and the BGPS (version 1.0.1) to construct a target sample for our class I methanol maser search. The properties of the two surveys are summarized below. The BGPS¹ is a 1.1mm continuum survey of 170 square degrees of the Galactic Plane in the northern hemisphere with the Bolocam instrument (Glenn et al. 2003; Haig et al. 2004), employed on the Caltech Submillimeter Observatory (CSO). Two distinct portions were included in the survey: a blind survey of the inner Galaxy region spanning $-10^\circ < l < 90^\circ$ where $|b| \leq 0.5^\circ$ everywhere, except for 1.0° cross-cuts at $l = 3^\circ, 15^\circ, 30^\circ,$ and 31° where $|b| \leq 1.5^\circ$, and a targeted survey towards known star formation regions in several outer Galaxy regions, including Cygnus-X ($70^\circ < l < 90.5^\circ, |b| \leq 1.5^\circ$), the Perseus Arm ($l \sim 111^\circ, b = 0^\circ$), the W3/4/5 region ($l \sim 135^\circ, b \sim 0.5^\circ$), IC1396 ($l \sim 99^\circ, b \sim 3.5^\circ$) and the Gemini OB1 molecular cloud ($l \sim 190^\circ, b \sim 0.5^\circ$). The

¹See http://irsa.opac.caltech.edu/data/BOLOCAM_GPS

survey detected approximately 8400 sources with an rms noise level in the maps ranging from 30 to 60 mJy beam⁻¹. The details of the survey methods and data reduction are described in Aguirre et al. (2011), and the source extraction algorithm and catalog (v1.0 BGPS data) are described in Rosolowsky et al. (2010). The effective FWHM beam size of the BGPS is 33", corresponding to a solid angle of 2.9×10^{-8} steradians, which is equivalent to a tophat function with a 40" diameter ($\Omega = 2.95 \times 10^{-8}$). Thus the BGPS catalog presents aperture flux densities within a 40" diameter aperture ($S_{40''}$), corresponding to the flux density within one beam. The BGPS catalog also provides an integrated flux density (S_{int}), which is the sum of all pixels within a radius (R also given in the catalog) of the BGPS source. Dunham et al. (2010) suggested that a correction factor of 1.5 must be applied to the Rosolowsky et al. BGPS catalog flux densities. This factor is based on a comparison of BGPS data with previous 1.2 mm data acquired with the MAMBO and SIMBA instruments (Aguirre et al. 2011). In this paper, we have also applied this correction factor to the flux densities in the Rosolowsky et al. BGPS catalog. The BGPS catalog includes the coordinates of both a geometric centroid and of the peak of the 1.1 mm emission. We have used the peak positions for the dust continuum emission (rather than centroid positions) in our analysis.

The Galactic Legacy Infrared Mid-Plane Survey Extraordinaire (GLIMPSE)² is a legacy science program of the *Spitzer Space Telescope* in a number of mid-infrared wavelength bands at 3.6, 4.5, 5.8, and 8.0 μm using the Infrared Array Camera (IRAC; Benjamin et al. 2003; Churchwell et al. 2009). The survey resolution is better than 2" in all wavelength bands. The survey catalogs for GLIMPSE I and II have been released. The GLIMPSE I survey covers $10 \leq |l| \leq 65^\circ$ with $|b| \leq 1^\circ$, and the GLIMPSE II survey covers the region of $|l| \leq 10^\circ$ with $|b| \leq 1^\circ$ for $|l| > 5^\circ$, $|b| \leq 1.5^\circ$ for $2^\circ < |l| \leq 5^\circ$, and $|b| \leq 2^\circ$ for $|l| \leq 2^\circ$. The data products include both highly reliable point source catalogs, and less reliable but more complete point source archives. In our analysis, we have used only the highly reliable point source catalogs from the GLIMPSE I and II surveys. The total area of the GLIMPSE I and II surveys is 274 square degrees. The overlap region between the BGPS and the two GLIMPSE surveys is $-10^\circ < l < 65^\circ$, $|b| < 0.5^\circ$ and $|b| < 1.0^\circ$ at $l = 3^\circ, 15^\circ, 30^\circ$, and 31° . We have used data from the overlap region to compile a sample of target sources to search for class I methanol masers.

The target sample was constructed by applying the following criteria: (1) A GLIMPSE point source with $[3.6]-[4.5]>1.3$, $[3.6]-[5.8]>2.5$, $[3.6]-[8.0]>2.5$ and an 8.0 μm magnitude less than 10; (2) the point sources meeting this mid-IR criterion must have a 1.1 mm BGPS counterpart within 15" (half the beam size of the BGPS survey); (3) the source must be at

²<http://irsa.ipac.caltech.edu/data/SPITZER/GLIMPSE/>

a declination greater than -25° (so as to be accessible to the PMO 13.7-m telescope); (4) the separation of each target source from all other target sources must be greater than half the beam size of the PMO 13.7-m telescope at 95 GHz ($30''$) (where this is not the case the source with stronger $4.5 \mu\text{m}$ emission is retained in the sample). The mid-IR criteria for selecting the initial sample of GLIMPSE point sources are based on the observed colors of known class I and class II methanol masers (see Figures 15, 16 and 18 of Ellingsen (2006)). Although Chen et al. (2011) found that some class I methanol masers are associated with GLIMPSE point sources with less-red colors ($[3.6]-[4.5]\sim 0.5$), the detection rates are highest for redder colors and so these criteria should be more efficient. When cross-matching the GLIMPSE point sources and the BGPS sources we only considered the separation between the GLIMPSE point source position and the BGPS peak position. We did not consider the measured size of the BGPS source, even though this method may miss some true associations between GLIMPSE and BGPS sources.

Within the BGPS-GLIMPSE overlap regions a total of ~ 420 GLIMPSE point sources satisfied the four criteria outlined above. Of these a total of 214 (approximately half) were randomly picked as the initial target sample for our 95 GHz class I methanol maser survey with the PMO 13.7-m telescope. Table 1 lists the target sample source parameters including the mid-IR magnitudes of the GLIMPSE point sources and the main parameters of the BGPS sources (including the BGPS ID number) extracted from the relevant catalogs used in this study. The separation between the GLIMPSE point source and the BGPS source range from $0.3''$ to $14.7''$ with a mean of $7.3''$. A histogram of the separations is shown in Figure 1.

2.2. Observations

The observations of the $8_0 - 7_1 \text{ A}^+$ (95.1964630 GHz) class I methanol maser transition were made using the PMO 13.7 m telescope in Delingha, China during 2011 March – April. We used the position of the 1.1 mm BGPS source peak emission rather than GLIMPSE point source as the target position for the observations. The positions of the target sources in Equatorial Coordinates (J2000) are given in Table 2. A new cryogenically cooled 9-beam SIS receiver (3×3 with a separation of $174''$ between the centers of adjacent beams) was used for the observations. This receiver operates in the 80–115 GHz band and the central beam of the 9 beam receiver was pointed at the target position. The system temperature for the observations was in the range 105–140 K, depending on the weather conditions and the atmospheric absorption τ was typically 0.15 – 0.2. A Fast Fourier Transform Spectrometer (FFTS) with 16384 spectral channels across a bandwidth of 1 GHz (corresponding to a

velocity range of $\sim 3000 \text{ km s}^{-1}$) was available for each beam during the observations. This gives an effective velocity resolution of 0.19 km s^{-1} for the 95 GHz class I methanol masers. However we only searched for maser emission over the velocity range from -200 to 200 km s^{-1} to cover the range of observed molecular gas in the Milky Way. Each source was observed in a position-switching mode with off positions offset $10'$ in right ascension. The pointing rms was better than $5''$. The standard chopper wheel calibration technique was applied to measure an antenna temperature, T_A^* corrected for atmospheric absorption. The FWHM beam size of the telescope is approximately $53''$ at this frequency with a main beam efficiency η_{mb} of 46%. The antenna efficiency is 42%, thus resulting in a factor of 45 Jy K^{-1} for conversion of antenna temperature into flux density. The initial observations had an on-source integration time of 10 mins for each of the 214 targeted sources yielding a T_A^* 1σ noise level of about 20 mK (corresponding to about 1.0 Jy) for each beam after Hanning smoothing of the spectra. Then, depending on the intensity of any detected emission we observed for an additional 10-20 minutes (on-source) to improve the signal-to-noise (SNR) of the final spectra. This yielded a typical rms noise level of 15 – 20 mK in the T_A^* scale (corresponding to 0.7 – 1.0 Jy) after Hanning smoothing. The corresponding rms noise (σ_{rms}) for each target source is summarized in Table 2.

The spectral data were reduced and analyzed with the GILDAS/CLASS package. Although data from all 9-beams were recorded, the locations of the 8 offset beams rotate with changing azimuth/elevation during the observation, thus only data from the central beam which was placed on the target position is valid. We only focus on the data from the central beam in this work. As part of the processing a low-order polynomial baseline fitting and subtraction, and Hanning smoothing were performed for the averaged spectra. Usually the 95 GHz methanol spectra do not have a particularly Gaussian profile, possibly because the spectra consist of multiple maser features within a similar velocity range. However, to characterize the spectral characteristics of the emission we have performed Gaussian fitting of each feature for each detected source.

3. Results

3.1. Class I methanol maser detection

95 GHz class I methanol emission above $3 \sigma_{rms}$ was detected toward 63 of the 214 targeted sources, corresponding to a detection rate of 29% for this survey. The spectra of the 63 detected class I methanol sources are shown in Figure 2. The detected objects are listed, along with the parameters of Gaussian fits to their 95 GHz spectral features in Table 3. The flux densities of the detected emission derived from the Gaussian fits range from \sim

0.6 to 43.4 Jy (corresponding to main beam temperatures $T_{BM} \sim 0.03$ to 2.1 K). The flux densities obtained from integrating the emission over all spectral features for each source are also given in Table 3 and range from 3 to 136 Jy km s⁻¹, with a mean of 24 Jy km s⁻¹. The measured FWHM of individual spectral features derived from Gaussian fitting are in the range 0.18 – 11.5 km s⁻¹ with a mean of 2.1 km s⁻¹. The spectra of the class I methanol emission in most sources usually include one or more narrow spectral features (typical line width <1 km s⁻¹ seen in Table 2) which are clearly maser emission (see Figure 2), but the same spectra often also contain broader emission features (typical line width >1 km s⁻¹ seen in Table 2). The pattern of class I methanol transitions containing both strong narrow spectral features and weaker broader emission has been seen in all previous single-dish surveys (e.g. Ellingsen 2005 and Chen et al. 2011), and their nature was discussed in detail by Chen et al. (2011). There are 13 sources which show a single broad Gaussian profile with a width of > ~ 2 km s⁻¹ (sources N20, N29, N32, N41, N78, N94, N99, N102, N117, N148, N154, N164 and N194; see Figure 2). At present our single-dish observations can not distinguish from their characteristics whether these broader emission sources are maser or thermal. For the purposes of our subsequent analysis we have assumed that some of the detected 95 GHz emission in these single broad line sources arises also from masers, recognising that future interferometric observations are required to determine whether or not this is correct. One point to note is that even if these single broad line sources are found to be purely thermal, the number (only 13) of these sources is too small to affect most of the statistical conclusions drawn in Section 4.

3.2. Comparison with previous detections

Among the 63 detected 95 GHz methanol sources, 20 have previously been detected as class I methanol masers in one or more transitions. The previous class I maser observations of these 20 sources are summarized in Table 4, including information as to which transitions have been detected. Table 4 shows that 12 of these sources (all of them are EGOs) have previously been detected in the 95 GHz transition, 11 of them by Chen et al. (2011) (Mopra EGO survey) and the other one from the survey of Val'tts et al. (2000). Twelve sources were also detected in the 44 GHz transition, including 6 EGOs detected by Cyganowski et al. (2009) and Slysh et al. (1994) as well as 6 sources from other surveys. Therefore 51 new 95 GHz class I methanol maser sources have been found in this survey, of which 43 are newly-identified as class I methanol maser sources. One source (source number N22 in our survey) was detected as a class I methanol maser at 44 GHz, but undetected at 95 GHz in a survey with the Nobeyama 45-m telescope by Fontani et al. (2010). While in our observations we detected emission in the 95 GHz transition with a peak flux density of ~ 12

Jy. We have compared the targeted positions for this source in the two surveys, and found that there is an angular separation of $\sim 18''$ between the targeted positions used. If the 95 GHz methanol maser emission detected in our PMO-13.7 m observations is located close to our targeted position, the non-detection with the Nobeyama 45-m telescope may be due to the relatively smaller beam size at 95 GHz ($18''$) which may not have covered the maser emission region in this case.

We have compared the spectra of the 11 sources which were detected in both the EGO-based Mopra survey (Chen et al. 2011), and in the current PMO 13.7-m survey. The two spectra overlaid are shown in Figure 3 and it can be clearly seen that the line profile and velocity range of each source are similar in both surveys. The observed emission intensities are consistent in 4 sources (N43, N73, N76 and N83), but are different in other 7 sources. Usually the emission detected in the current PMO survey is (1.5 – 2 times) stronger than that in the previous Mopra survey (except for one source N97 with stronger emission detected in the Mopra survey). In addition to flux density calibration uncertainties between the two telescopes, the following factors may cause the observed difference in the detected emission intensity between the two surveys: 1) different target positions were adopted in the two surveys; 2) the different beam sizes of the telescopes used in the two surveys cover different regions; 3) intrinsic intensity variability in the class I methanol maser emission between the two epochs. We have compared the targeted positions used in the two surveys, and found that the angular separation typically ranges from $1''$ to $10''$ in both the sources with and without a significant difference in the observed intensity, thus it does not seem that case 1 is the major factor in explaining the differences. Case 2 is plausible if the maser emission is extended to spatial scales comparable to, or larger than the Mopra beam ($36''$ at 95 GHz), in which case the PMO would detect additional maser emission outside the Mopra beam. This is consistent with the observed results in the two surveys for most sources, as stronger emission was detected by the PMO, but one source (N97) shows the opposite trend with stronger emission detected by the Mopra rather than the PMO. In this case one of possibilities is that there is intrinsic intensity variability in this source, although we can not characterise the nature of the variations with only two epochs of data collected using different telescopes. Moreover the exact coordinates of this source are unknown, so it is possible that both in the Mopra and PMO observations are at an offset position, in which case even a fairly small difference in the telescope pointing of about $10''$ can lead to a higher intensity observed with a narrower beam (Mopra) than with a broader beam (PMO), provided that Mopra was pointing more directly towards the source. Variations in the intensity of 6.7 GHz class II methanol masers have been detected with timescales on the order of days to years (e.g. Goedhart et al. 2004; Ellingsen 2007; Goedhart et al. 2009; Szymczak et al. 2011) and some sources have been found to exhibit periodic variability (e.g. Goedhart et al. 2009;

Szymczak et al. 2011). Intensity variation in class I methanol masers has also been reported in a few sources (e.g. Kurtz et al. 2004; Pratap et al. 2007), but to date there are no systematic observations of class I methanol maser variability. It will be necessary to perform multi-epoch observations with accurate calibration to determine the characteristics of the intensity variations in class I methanol masers.

3.3. Distance and luminosity of class I methanol masers

The distance and the distance-dependent integrated maser luminosity for each of the 63 detected methanol maser sources are given in Table 5. We used the Galactic rotation model of Reid et al. (2009), with the Galactic constants set to, $R_{\odot} = 8.4$ kpc and $\Theta_{\odot} = 254$ km s⁻¹ to estimate the distances. Since class I methanol maser emission is generally observed to lie close to the V_{LSR} as measured from the thermal gas (e.g. Cyganowski et al. 2009), the velocity of the brightest feature in the 95 GHz maser spectrum was used in the distance calculation. All Galactic rotation models suffer from ambiguity (known as kinematic distance ambiguity) for sources which lie within the solar circle. With the exception of the velocity associated with the tangent point, there are two distances (referred to as a near and far distance), either side of the tangent point, which will produce the same line-of-sight velocity. All of the sources with 95 GHz methanol masers detected in our survey fall within the solar circle. Where present, an association between the detected class I methanol maser source and an infrared dark cloud (IRDC) may allow us to resolve the distance ambiguity. IRDCs are believed to represent sites where the earliest stages of massive star formation are present (e.g. Egan et al. 1998; Carey et al. 1998, 2000; Simon et al. 2006a, 2006b). They are observed in absorption against the diffuse infrared background especially at 8.0 μ m, and hence the identification of IRDCs is greatly biased toward nearby sources (and hence the near kinematic distance), where they will show greater contrast against the diffuse IR background (see Jackson et al. 2008). We have cross-matched the 63 detected 95 GHz methanol masers with the catalog of IRDCs seen in the *Spitzer* GLIMPSE images (Peretto & Fuller 2009), and we have undertaken visual inspection of the GLIMPSE 8 μ m images for those sources with $|l| < 10^{\circ}$ (which are not included in Peretto & Fuller catalog). The information as to whether the class I methanol maser detections are associated with IRDCs or not is summarized in Column (8) of Table 5. We found 33 of 63 maser sources for which the associated BGPS sources are spatially coincident and structurally similar to IRDCs. We have assumed that these 33 sources are at the near kinematic distance. The remaining 30 class I maser sources are associated with BGPS which are not coincident with IRDCs, and for these we have adopted the far kinematic distance.

To examine how reasonable (or otherwise) the above distance assumptions are, we have cross-checked our distance determinations for a subsample of class I maser sources for which the distance ambiguity has been resolved in other studies. Some of our detected class I maser sources have a class II methanol maser association (see Section 4.3 for the identification of the class II maser associations), and some of these have had the distance ambiguity more directly resolved using HI self-absorption (HISA) from the Southern Galactic Plane Survey (SGPS) or the VLA Galactic Plane Survey (VGPS) by Green & McClure-Griffiths (2011). We found that 9 of the 10 sources with IRDC associations (which we assume to be at the near distance) are assigned the near distance by Green & McClure-Griffiths (2011), and 5 out of the 6 sources without IRDCs (which we assume to be at the far distances) are assigned to be at the far distance by their work. We have marked these sources with a “G” in Table 5, and adopted the distances from their work in our analysis for these sources. Moreover some of our detected class I maser sources are included in the sample of BGPS sources studied with molecular lines (e.g., NH_3 , HCO^+ and N_2H^+) by Dunham et al. (2011b) and Schlingman et al. (2011). There are 16 sources (marked by “S” in Table 5) which are contained in the BGPS sample with distances determined in Table 5 of Schlingman et al. (2011). Among them 14 sources have distance solutions determined from Galactic rotation (the other two sources N194 and N210 have no reliable distance estimations from the Galactic rotation; see below), and our distance determinations with the IRDC method for them (including 13 sources with IRDC associations at near distance, and 1 source without IRDC associations at far distance) are consistent with that determined in Schlingman et al. (2011). The 9 sources (marked by “D” in Table 5) are included in the BGPS sample with distances determined in Table 6 of Dunham et al. (2011b). Comparing their distances with those estimated from our analysis on the basis of the presence or otherwise of an IRDC (7 sources with and 2 sources without IRDCs, respectively) are also generally consistent with those estimated by Dunham et al. (2011b). In addition, one point to note is that the identification of an IRDC depends on the presence of a bright $8\ \mu\text{m}$ infrared background, so a source at the near distance without a significant infrared background might be not identified as IRDC. Therefore for those sources without an identified IRDC, the distance may be less certain and biased toward large distances. The reliability of the distance determinations for our sources without IRDC associations could potentially be improved through additional HISA investigations, however, Dunham et al. (2011b) find that HISA is unlikely to be present for BGPS sources without an associated IRDC. They find that for 215 BGPS sources without IRDC identifications listed in Table 6 of Dunham et al. (2011b), only 26 present a definite HISA features. Hence, we have not undertaken any additional HISA determinations beyond those already available in the literature, as the available cross-checks show that our assumption of the near and far kinematic distances for sources with and without IRDCs respectively appear reasonable. The accuracy of this discriminator for kinematic distances can’t be accurately assessed with

such a small sample, however, if our results are representative then it is at $\sim 90\%$. In some cases the Galactic rotation model is not able to provide a reliable distance estimate and for these sources (sources N33, N194 and N210 in Table 1) we have adopted a distance of 4 kpc for source N33 (which has an IRDC association), and that determined by Schlingman et al. (2011) for the other two sources N194 and N210.

Based on the estimated distances, the integrated luminosity of 95 GHz methanol maser, L_m can be calculated from $L_m = 4\pi \cdot D^2 \cdot S_{int}^m$, where D is the estimated distance and S_{int}^m is the integrated flux density of the 95 GHz emission. This assumes that maser emission is isotropic, which is known to be false, however, in the absence of any information on the beaming angle of the maser emission, nor our alignment with respect to it, this is the only feasible approach that can be undertaken.

4. Analysis and Discussion

4.1. Mid-IR characteristics of GLIMPSE point sources

Analysis of the mid-IR colors of GLIMPSE point sources associated with EGOs with and without class I methanol maser detections has been performed by Chen et al. (2011). No significant difference in the mid-IR colors was found between the GLIMPSE point sources with and without class I methanol masers in the EGO sample (see Figure 5 of their work). We have performed the same analysis for our observing sample to further investigate the mid-IR characteristics of the GLIMPSE point sources which are, and are not, associated with class I methanol masers. Although the detected class I maser sources in our PMO survey include 12 EGOs which were considered in the color analysis by Chen et al. (2011), the remaining 51 newly-discovered 95 GHz class I methanol maser sources (which includes 3 EGO associated sources previously only detected in the 44 GHz transition) allows us to explore in a more unbiased manner, the mid-IR characteristics of GLIMPSE point sources associated class I methanol masers.

A number of color-color diagrams were constructed to compare the mid-IR colors of the GLIMPSE point sources with and without an associated class I methanol maser detection in our survey. In Figure 4 we plot three color-color diagrams ($[3.6]-[4.5]$ vs. $[5.8]-[8.0]$; $[3.6]-[5.8]$ vs. $[3.6]-[8.0]$ and $[3.6]-[4.5]$ vs. $[4.5]-[8.0]$) using different symbols for the sources which are, and which are not associated with class I methanol masers. There are 63 members of the group associated with class I methanol masers and 151 members of the group which are not associated with class I methanol masers. This figure shows that there are no clear differences in the mid-IR colors between those sources in our sample which are associated

with a class I maser, and those which are not, consistent with the findings from the EGO-based sample of Chen et al. (2011). There are 15 sources in total associated with known EGOs in our observing sample (see Table 4). The color regions occupied by the sources at evolutionary Stages I, II and III, (derived from the 2D radiative transfer model of Robitaille et al. (2006)), are marked on the [3.6]-[4.5] vs. [5.8]-[8.0] color diagram of Figure 4 (left panel). We found that most (187/214) sources in our observed sample fall in the region occupied by the youngest protostars (Stage I), with the remaining 27 sources found in the upper-left of the color-color diagram, outside the Stage I evolutionary region. Chen et al. (2011) have discussed these redder GLIMPSE sources which lie outside the Stage I color region in detail. They may be deeply reddened sources (with reddening vector $A_v \sim 80$; a typical reddening vector of $A_v=20$ derived from the Indebetouw et al. (2005) extinction law is shown in Figure 4 to demonstrate the reddening effect), MYSOs with an extremely high mass envelope, or caused by emission mechanisms such as H_2 or PAH line emission which were not included in the Robitaille et al. (2006) models. One of the most likely explanations is that they have excess $4.5 \mu\text{m}$ emission from shocked H_2 in particularly strong/active outflows, which in turn readily produces class I maser emission. This is supported by the high detection rate of class I methanol masers towards these redder sources seen in both the current observations (17/27=63% in this survey), and the EGO survey of Chen et al. (2011) (a detection rate of 75%). We discuss possible dependence of the detection rate of class I methanol masers with the colors or magnitudes of GLIMPSE point sources in greater detail in Section 4.4. For the redder GLIMPSE point sources (outside the Stage I region), 8 sources with an associated class I methanol maser are also associated with EGOs (marked by red triangles in Figure 4), which means the other 9 sources with an associated class I masers are not associated with an EGO, although 3 of them are associated with known MYSOs (sources N22, N90 and N101; see Table 4).

We have undertaken a detailed analysis of possible correlations between the class I methanol maser emission and the associated GLIMPSE point sources. Figure 5 (left panel) shows a log-log plot of the integrated luminosity of the class I methanol masers versus the luminosity of the GLIMPSE point sources in the $4.5 \mu\text{m}$ band. The distance to the source listed in Table 5 was used to calculate the luminosity for both the class I maser and the GLIMPSE point source (see the discussion of distance assignment in Section 3.3). A linear regression analysis for this distribution was undertaken, and the line of best fit obtained is plotted in the figure. Our analysis suggests that there is a statistically significant positive slope in the distribution, but with a weak correlation (the best fit shows a slope of 0.41 with a statistically significant p-value of 10^{-4} which allows us to reject zero slope in the data, and a low correlation coefficient of 0.47). Such a correlation seems reasonable if the $4.5 \mu\text{m}$ emission is believed to be enhanced by shocks, which are also thought to be responsible for

the class I methanol maser emission. On the other hand, this correlation may be simply a consequence of the correlation between the class I methanol maser and central source luminosity, which has been obtained by, e.g., Bae et al. (2011) for the 44 GHz masers. However, our determination of the distances using the presence or absence of an IRDC to resolve the distance ambiguity will introduce unpredictable uncertainties as discussed in Section 3. To eliminate the possible effects of distance dependencies in our investigations we compared mid-IR color [3.6]-[4.5] with [3.6]- $\log(S_m)$, where S_m is the integrated flux density of the class I methanol maser (a plot of this is shown in the right-hand panel of Figure 5). This plot shows no significant correlation between the “colors”, with the linear regression analysis giving a slope of 0.6, a non-significant p-value of 0.10 and a small correlation coefficient (0.22). One possible reason for weak or non-significant correlation between them is that the GLIMPSE point sources which have been identified as being associated with the class I methanol masers may not be the true driving sources. Within the large field-of-view covered by the PMO beam size (52”), there will always be a number of GLIMPSE point sources, and from the present observations with this resolution we can not determine which one is the driving source of the class I methanol maser. Our assumption that the GLIMPSE point source which satisfies the mid-IR color criteria for the class I maser search in our survey is the driving source is almost certainly wrong in some cases, indeed some driving sources of class I methanol maser are likely not present in the GLIMPSE point source catalog due to saturation, the presence of bright diffuse emission, or intrinsically extended morphology in the IRAC bands (e.g. from extended PAH emission or extended H₂ emission in shocked gas (see Robitaille et al. 2008, Povich et al. 2009, and Povich & Whitney 2010)). On the other hand, if the GLIMPSE point sources do correspond to the true driving sources of the class I methanol masers, the lack of significant correlations between the maser and GLIMPSE mid-IR colors suggests that the excitation of the class I methanol masers are not directly related to the mechanism responsible for the mid-IR emission. This view is supported by the fact that class I methanol maser spots are often distributed over large angular and spatial scales (usually of the order of 10”), and are excited in shocked regions (e.g. Cyganowski et al. 2009), whereas the GLIMPSE point sources emission reflects the thermal dust or molecular environments within a smaller region around the protostar. Moreover, the 4.5 μm emission may still be dominated by the thermal dust emission from the driving protostar, rather than the molecular gas (such as H₂ or CO) excited by shocks, thus masking any relationship between the class I methanol maser properties and the 4.5 μm intensity.

4.2. Relationships between class I methanol masers and BGPS sources

A close correlation between GLIMPSE point sources with an associated class I methanol masers and the presence of a 1.1 mm BGPS sources was first noted in the EGO-based survey of Chen et al. (2011), the analysis of which motivated the investigations undertaken here. Chen et al. showed that the luminosity of the class I methanol masers in the EGO sample strongly depends on the properties (including both the mass and volume density) of the associated 1.1 mm dust clump: the more massive and denser the clump, the stronger the class I methanol emission. Here we perform a similar analysis to Chen et al. (2011) on a sample of class I methanol masers which combines GLIMPSE point sources and BGPS sources to investigate the relationship between the dust clumps and the maser emission in a wider sample of sources.

Based on the assumption that the 1.1 mm emission from the BGPS source arises from optically thin dust, we can calculate the associated gas mass using the equation:

$$M_{gas} = \frac{S_{int}D^2}{\kappa_d B_\nu(T_{dust})R_d}, \quad (1)$$

where S_{int} is the 1.1 mm integrated flux density of the BGPS source, D is the distance to the source, κ_d is the mass absorption coefficient per unit mass of dust, $B_\nu(T_{dust})$ is the Planck function at temperature T_{dust} , and R_d is the dust-to-gas mass ratio. Here we have used $\kappa_d=1.14 \text{ cm}^2 \text{ g}^{-1}$ for 1.1 mm (Ossenkopf & Henning 1994) and a dust-to-gas ratio (R_d) of 1:100 in our calculations and $B_\nu(T_{dust})$ was calculated for an assumed dust temperature of 20 K. The average H_2 column density (N_{H_2}) and volume density (n_{H_2}) of each dust clump were then derived from its mass and radius (R), assuming a spherical geometry and a mean mass per particle of $\mu = 2.37 m_H$. The parameters of the 1.1 mm continuum integrated flux density, S_{int} and 1.1 mm source radius, R were obtained from the BGPS catalog (Rosolowsky et al. 2010) for the 214 sources in our sample and the values are listed in Table 1. We applied a correction factor of 1.5 to the Rosolowsky et al. BGPS catalog flux densities (which are also listed in Column (11) of Table 1 of our work) to derive the gas masses for the 63 BGPS sources with an associated class I methanol maser detection. For the two sources (sources N39 and N143) which are unresolved with the BGPS beam, we were not able to determine their gas column and volume densities due to the absence of the size of the BGPS source. The derived masses and gas densities for the 1.1 mm dust clumps with an associated class I methanol maser are given in Table 5. As stated in Section 3.3, there is a small number of detected class I maser sources which are also included in the sample of BGPS sources investigated by Dunham et al. (2011b) or Schlingman et al. (2011). Comparing the physical parameters (gas mass and volume/column density) derived for those BGPS sources which are in common with the two previous studies, we find that they are consistent with each

other (usually similar but not identical).

A log-log plot of the luminosity of the class I methanol maser versus the derived gas mass (left panel) and H₂ volume density (right panel) of the associated 1.1 mm BGPS source is shown in Figure 6. From this figure it can be seen that there is significant positive correlation between the class I maser luminosity and the gas mass of the BGPS source, while a very weak negative correlation exists between the class I maser luminosity and the H₂ volume density. Linear regression analysis for both distributions (the corresponding best fit lines are overlaid in each panel of Figure 6) find a statistically significant (p-value of 8.1E-13) linear dependence with a slope of 0.81 existing between the maser luminosity and the gas mass (the slope has a standard error of 0.07 and a correlation coefficient of 0.84). In contrast, there is no statistically significant correlation (p-value of 0.10) between the class I methanol maser luminosity and the gas density (the fit has a slope of -0.25 and a small correlation coefficient of 0.22). The statistically-significant positive correlation between class I maser luminosity and BGPS source mass obtained in this study is similar to that measured in the EGO-based sample of Chen et al. (2011). Chen et al. (2011) also found a weak but statistically significant positive correlation between the class I maser luminosity and the gas volume density in the EGO sample, however, no statistically significant or a very weak negative correlation is observed in our larger and more diverse sample.

We also carried out an investigation of the dependence between the BGPS beam-averaged gas column density and the class I methanol maser integrated flux density (both of which are independent of the assumed distance to the source). The H₂ column density per beam can be estimated by

$$N_{H_2}^{beam} = \frac{S_{40''}}{\Omega_{beam} \mu \kappa_d B_\nu(T_{dust}) R_d}, \quad (2)$$

where $S_{40''}$ is the 1.1 mm flux density within an aperture with a diameter of 40'', Ω_{beam} is the solid angle of the beam, μ is the mean mass per particle, κ_d is the mass absorption coefficient per unit mass of dust, $B_\nu(T_{dust})$ is the Planck function at temperature $T_{dust} = 20$ K, and R_d is the dust-to-gas mass ratio, as described above. $S_{40''}$ was adopted as the measure of the flux within a beam since a top-hat function with a 20'' radius has the same solid angle as a Gaussian beam with an FWHM of 33'' (see also Section 2.1). In addition to a flux correction factor of 1.5 (see above), an aperture correction of 1.46 should be applied to flux density $S_{40''}$ (which is given in Column (10) of Table 1 in our work) to account for power outside the 40'' aperture due to the sidelobes of the CSO beam (Aguirre et al. 2011) in the calculation of beam-averaged column density. Since this property is independent of the distance to the source, we can derive it for all BGPS sources in our sample and we have listed it for each source in Column (12) of Table 1. The results are shown as a log-log plot

in Figure 7 which demonstrates that there is a statistically significant positive correlation between the beam-averaged gas column density of BGPS sources and the integrated flux density of class I methanol masers (S_{int}^m). We have performed a linear regression analysis for this distribution and obtain a best fit linear equation of:

$$\log(S_{int}^m) = 0.75[0.10]\log(N_{H_2}^{beam}) - 15.94[2.28] \quad (3)$$

with a correlation coefficient of 0.69 and p-value of 3.25E-10. This relationship between the class I maser flux density and the beam-averaged gas column is important for refining future class I methanol maser surveys based on BGPS sources because it is independent of distance and other intrinsic physical parameters of the sources. For example, toward nearby low-mass star-forming regions a threshold column density of $123 M_{\odot} \text{ pc}^{-2}$ (corresponding to $6.5 \times 10^{21} \text{ cm}^{-2}$) has been observed (Lada et al. 2010; Heiderman et al. 2010), and substituting this into the above relationship we can estimate a lower limit of 2.6 Jy km s^{-1} for the integrated flux density of 95 GHz class I methanol masers. The lowest class I maser integrated flux density from our observations is only slightly higher ($\sim 3.0 \text{ Jy km s}^{-1}$), which suggests that we are likely to have detected significant part the 95 GHz class I maser sources in the observed sample.

4.3. Star formation activity associated with methanol masers

The star formation activity of the BGPS sources was characterized by Dunham et al. (2011a), through the properties of mid-IR sources along a line of sight coincident with the BGPS sources. They divided the BGPS sources into four groups representing increasing probability of the associated mid-IR sources indicating star formation activity. The sources with the highest probability of star formation activity are classified as group 3 and include BGPS sources matched with EGOs or Red MSX Survey (RMS; Hoare et al. 2004; Urquhart et al. 2008) sources. The lowest probability group (group 0) includes BGPS sources which were not matched with any mid-IR sources and are considered to be “starless” in their work. Groups 1 and 2 represent BGPS sources matched with GLIMPSE red sources cataloged by Robitaille et al. (2008), or a deeper list of GLIMPSE red sources created by Dunham et al. (2011a). Overall they found that the mid-IR emission associated with BGPS sources with a high probability of star formation activity (group 3) are typically extended with large skirts of emission, while the low probability sources (group 1) are more compact, with weak emission. In this section, we explore the star formation activity in the sources with and without methanol maser associations using the parameters of the BGPS sources.

Histograms of BGPS source parameters (beam-averaged H_2 column density $N_{H_2}^{beam}$, integrated flux density S_{int} and radius R) for those sources with and without an associated

class I methanol maser are presented in Figure 8. Unfortunately we are not able to compare any intrinsic physical parameters such as mass, source size in pc etc between the two groups, due to the absence of a distance estimate for the sources without an associated class I methanol maser. For each distribution in Figure 8, the upper and lower panels correspond to the BGPS sources with and without a class I maser detection, respectively. It can be clearly seen that the distributions differ significantly between BGPS sources with an associated class I maser and those without for the beam-averaged H_2 column density and the integrated flux density of BGPS sources (see left-hand and middle panels). In contrast there is no significant difference in the observed distribution of the radius of the BGPS sources for the two samples (see right-hand panel). The basic statistical parameters such as mean, median, standard deviation, for each of these distributions are summarized in Table 6. The mean logarithm of the beam-averaged column density $N_{H_2}^{beam}$ is 21.9 [cm^{-2}] for the sources with no class I methanol maser detections, but 22.7 [cm^{-2}] for the sample of sources with an associated class I methanol maser (a difference of approximately 3 standard deviations). While the mean logarithm of the BGPS integrated flux density is 0.0 [Jy] in sources without an associated class I masers, but greater at 0.7 [Jy] in sources with class I masers (a difference of approximately 2 standard deviations). However, a t -test finds that the difference in the mean of each of the distributions for these two properties is statistically significant for the two groups. The distributions of radii are not significantly different between the two groups, each having a mean of around $50''$ and a large range (mostly distributed between 20 and $100''$). The beam-averaged column density for the BGPS sources without an associated class I maser ranges between $21.4 [\text{cm}^{-2}] \leq \log(N_{H_2}^{beam}) \leq 22.7 [\text{cm}^{-2}]$, whereas for sources with an associated class I masers the range is $21.9 [\text{cm}^{-2}] \leq \log(N_{H_2}^{beam}) \leq 23.8 [\text{cm}^{-2}]$. Similarly the range of the logarithm of integrated flux density is from -0.9 to 1.1 [Jy] for BGPS sources without an associated class I masers, but from -0.6 to 1.5 [Jy] for those with a class I masers. The large overlapping range in the integrated flux density distribution of the two groups suggests that the beam-averaged column density is the most efficacious parameter for selecting BGPS sources likely to be associated with a class I methanol maser.

Comparing the distribution of the beam-averaged H_2 column density for the four star formation activity groups described by Dunham et al. (2011a; Figure 12), with that for the class I methanol maser sample we can see that it is similar to that shown for group 3. While the distribution for the sources without an associated class I methanol maser is similar to that seen for group 0 and group 1 by Dunham et al. Comparing distributions of BGPS source flux for our samples with Dunham et al. (2011a), those without class I masers appear to agree well with their group 1. As described above, group 3 contains the sources with the highest probability of star formation activity include BGPS sources matched with EGOs or RMS sources, while group 0 represents those with the lowest probability, including BGPS sources

without any associated mid-IR source (referred as “starless”). Since all of our target BGPS sources have an associated GLIMPSE point source we would expect that the distributions we observe should differ from those seen for group 0 sources, which have no associated mid-IR source. The group 1 category sources include at least one IR object which may be an AGB star catalogued by Robitaille et al.(2008) or a deeper GLIMPSE red source from the list of Dunham et al. The BGPS sources in our sample with an associated class I masers (63 in total) includes 15 EGOs (which are classified into group 3 by Dunham et al.), however, the relatively small number of EGOs can not dominant the BGPS parameter distributions observed for this group. The remaining 48 sources must also have a similar BGPS parameter distribution to that observed for group 3. Since class I methanol maser emission is only known to be found towards active star formation regions, the similar distribution of the BGPS properties seen in the class I maser sources and the group 3 sources supports the speculation of Dunham et al. (2011a) that group 3 sources are those with the highest probability of star formation activity. The BGPS sources in our target sample without an associated class I methanol maser, correspond to group 1 in the Dunham et al. classification (which have a lower probability of star formation activity), and these may be regions which are either too young, or have too low gas density, or too weak outflows to excite class I maser emission. Comparing our observing sample with the GLIMPSE red source catalog compiled by Robitaille et al. (2008), we found that there are 95 sources are common in the two data sets (including 22 sources with class I masers and 73 sources without class I masers). Using the criteria of Robitaille et al. to separate AGB stars and YSOs, 8 of 22 sources for which we have detected an associated class I masers are classified as extreme AGB stars with high mass-loss rates and therefore significant circumstellar dust. However, since class I methanol masers appear to only be associated with star formation, this suggests that there may be a relatively high mis-classification rate for the extreme AGB sources using the Robitaille et al. criteria. We found that only 9 of 73 BGPS sources from our sample which are not associated with class I masers are classified as AGB stars. This also supports the hypothesis that the sources without class I masers may be objects at early stages of star formation, rather than AGB stars.

Analysis of the properties of 1.1 mm BGPS associated with EGOs by Chen et al. (2011) showed that those which are associated with class I methanol masers, but not class II methanol masers have a lower mass/density of dust clump than those which are associated with both class I and II methanol masers. We have cross-matched the 63 sources with an associated class I methanol maser detected in our survey with the catalog of 6.7 GHz class II methanol masers (usually better than 1”) from the Parkes Methanol Multibeam (MMB) blind survey published to date (Caswell et al. 2010; Green et al. 2010 ; Caswell et al. 2011 ; Green et al. 2012), or from the ATCA observations of Caswell (2009). The MMB masers po-

sitions have been measured to high positional accuracy (better than $1''$) and the observations have a sensitivity of about 0.2 Jy (3σ from the subsequent ATCA observations). The MMB survey published to date covers the region $186^\circ < l < 20^\circ$ with $|b| < 2^\circ$. Thus the overlap region between the class I methanol maser sources detected in our survey and the class II methanol masers in the MMB survey is $0^\circ < l < 20^\circ$ with $|b| < 0.5^\circ$. The MMB survey data from the overlap region allow us to identify the associations between the two classes of methanol masers, and in particular to identify those class I methanol maser sources without an associated class II masers. Whether the class I methanol maser detected in this survey is associated with a class II maser or not is summarized in Column (9) of Table 5. Thirty three of the 63 class I methanol masers in our sample lie in the MMB overlap region and Caswell (2009) data set, and of these 20 have an associated class II maser and 13 do not. Histograms of the beam-averaged H_2 column density and flux density of BGPS for the sources associated with only class I methanol masers compared to those associated with both classes of methanol maser are shown in Figure 9. Although the sample sizes for the two groups are relatively small, they still allow us to investigate whether the BGPS properties discriminate between the two groups. The statistical parameters for each distribution are summarized in Table 6. From Figure 9 and the statistical parameters we can see that there is a trend for the sources associated both methanol maser classes to have higher BGPS flux densities and column densities than the sources associated with only class I masers. The mean column density and flux density of the associated BGPS sources are marked with a dashed line in the corresponding histogram, and are significantly larger for the sample of sources associated with both classes of methanol maser. A t -test shows that the difference in the mean of the two group distributions for the two BGPS properties is statistically significant.

It is important to note that the sample size used in the current analysis is small. A larger sample is required to more thoroughly investigate the star formation activity and physical properties of the regions with associated class I and II methanol masers. In addition, our assumption of a dust temperature (T_{dust}) of 20 K for all sources in our analysis will affect the physical parameters such as mass and column/volume density derived from the BGPS data. For example, a dust temperature of 7.2 K for the BGPS sources with an associated class I methanol maser and a dust temperature of 20K for those without would result in distributions of the beam-averaged column density for the two samples having the same mean. However, the mean gas kinetic temperature derived from the NH_3 observations for group 3 sources (those similar to the class I maser group) was 22.7 K (Dunham et al. 2011b), much higher than the 7.2 K required to give the distributions the same mean. Furthermore, since the BGPS sources without an associated class I maser are similar to group 1 of Dunham et al., for which the mean temperature from NH_3 observations is 14.6 K (Dunham et al. 2011b), the expectation is that more accurate temperature estimates for individual BGPS sources

would produce a greater difference in the distributions of the physical properties derived from BGPS data, rather than reducing it.

4.4. Detection rates

In this section, we compared the detection rates of class I methanol masers with the cataloged parameters of the associated GLIMPSE point sources and 1.1 mm BGPS sources with the aim of developing more efficient criteria for future targeted class I methanol maser searches.

Figure 10 presents a histogram showing the detection rate of class I methanol masers as a function of the $4.5 \mu\text{m}$ magnitude (left panel) and $[3.6]-[4.5]$ color (right panel) of the associated GLIMPSE point sources. It can be clearly seen that the detection rate for class I masers increases (from 0.1 to 0.5) as the $4.5 \mu\text{m}$ magnitude decreases (i.e. with increasing $4.5 \mu\text{m}$ flux density). In contrast the detection rate for class I methanol masers shows no significant variation for $[3.6]-[4.5]$ color < 3.2 , being $\sim 0.2 - 0.3$, however for $[3.6]-[4.5] > 3.2$ it is much higher (0.8–1.0). Recalling the discussion in Section 4.1, these results are consistent there being no significant differences between the mid-IR colors of the sources with and without an associated class I methanol maser, however, there is a higher detection rate for class I methanol masers towards GLIMPSE point sources with the most extreme red range for $[3.6]-[4.5]$ color. Chen et al. (2011) have suggested that these redder sources may correspond to higher mass, high luminous YSOs. The correlation between the detection rate of class I methanol masers and the $4.5 \mu\text{m}$ magnitude (or flux density) of the associated GLIMPSE point source suggests that the outflows or shocks are stronger or more active for those with more intense $4.5 \mu\text{m}$ emission which thus are more likely to produce maser emission. Apart from correlation between the emission intensities of class I methanol masers and the GLIMPSE $4.5 \mu\text{m}$ band (Figure 5, left), there is clearly an increased probability of the presence of a methanol maser for sources with stronger $4.5 \mu\text{m}$ emission. This may be because although strong $4.5 \mu\text{m}$ emission is a good indicator of the presence of shocks (and hence the possibility of a class I maser), the intensity of the maser may depend more strongly on other physical factors such as the gas mass and column density of the parent clouds. We also note that while sources with $[4.5] < 8.0$ have a higher detection rate for class I methanol masers (0.4 – 0.5), they were typically classified as extreme AGB stars by Robitaille et al. (2008). At present all class I methanol masers are thought to be associated with star formation, which suggests that there is a high mis-classified rate for the extreme AGB star population in Robitaille et al. (2008) and that many of these sources correspond to luminous YSOs.

The detection rates of class I methanol masers as a function of the BGPS cataloged parameters (beam-averaged H_2 column density and integrated flux density) are shown in Figure 11. The BGPS radius parameter is not included in the analysis because as discussed in section 4.2, the radius is the least useful BGPS parameter in terms of its ability to select BGPS sources with a higher likelihood of having associated class I maser emission. From this figure, we can clearly see that the detection rates for class I methanol masers significantly increase with increasing values of the BGPS source parameters. To allow a more detailed comparison the number and rate of detection for class I masers in each bin for each BGPS parameter in our observed sample and the full BGPS catalog are summarized in Table 7. This shows that the detection rate for this sample is 100% for sources with the highest beam-averaged column density (larger than $23.0 \text{ [cm}^{-2}]$ in logarithm) and BGPS integrated flux density (larger than 1.2 [Jy] in logarithm). We note that if there are thermal sources among the objects detected at 95 GHz, they may be preferentially associated with BGPS sources with the highest column densities. As the number of these BGPS sources in the high column density bins is small, even a few sources can potentially distort the statistics. To test for this we excluded the 13 (potentially thermal) sources with a single broad line profile (as identified in Section 3.1), from the class I methanol maser detection sample and from the total sample and redid our analysis. Our re-analysis excluding potential thermal sources showed a similar trend to that seen in Figure 11. In fact, among the 13 broad line profile sources, only 3 are located in the high column density bins ($> 10^{23} \text{ cm}^{-2}$) with 100% probability of a 95 GHz maser detection. Thus the possible thermal 95 GHz sources do not precisely correspond to BGPS sources with the highest column densities. The rate (3/9) of the possible thermal sources to the class I methanol detection sources in the high column density bins is relatively low, thus the possible thermal sources do not significantly distort the statistics. Moreover, as stated in Section 3.1, we can not exclude the possibility that the emission from weak maser features contributes to the broad line profiles. Our analysis using all 95 GHz detections does not exclude any possible maser sources for a future survey toward a larger BGPS sample (see below). Even if we assume that all the broad line profile sources are totally thermal, the rate of real maser sources would still be very high (50/63=80%) in any sample derived on the basis of all 95 GHz detections.

For class I methanol maser surveys with a single dish with a beam size of around an arcminute, it seems that the millimetre continuum emission on similar scales (e.g. the BGPS sources) can provide a better targeting criteria than the arcsecond-scale mid-IR emission (e.g. GLIMPSE point sources). Our earlier discussion shows that the class I methanol maser emission intensity is not closely related to the mid-IR emission of GLIMPSE point sources, but does depend on the mass and beam-averaged column density of the associated BGPS sources, also suggesting that BGPS properties are likely to provide a better basis

for constructing samples for further class I methanol maser searches. We also undertook binomial generalized linear modeling (GLM) for the class I maser presence and absence using both the GLIMPSE point source and BGPS properties, similar to that undertaken for water masers by Breen et al. (2007) and Breen & Ellingsen (2011). This investigation showed that the BGPS source properties are a much stronger predictor of the likelihood that a particular source will host a maser, than are the mid-IR properties, consistent with the investigations outlined above. As the results of the binomial GLM are less readily interpreted than the more direct correlation investigations in sections 4.1, 4.2 and 4.3, and don't reveal any significant new information we do not discuss them further here.

To more efficiently search for class I methanol masers using the BGPS sources, we can combine the two BGPS properties of beam-averaged column density and integrated flux density to develop better criterion for future searches. In Figure 12 (left panel) we plot a log-log distribution comparing the BGPS flux density versus BGPS beam-average column density from the current observations using different symbols for the sources with and without class I methanol maser detections (including also possible thermal sources). This clearly shows that there is a significant discrimination between sources with class I masers (marked by red circles) and those without class I masers (marked by blue triangles). From inspection of this plot we have defined a region wherein most (90%) of class I methanol maser detected in our current survey are placed, constructed with red lines in the plot. The defined region can be expressed as follows:

$$\log(S_{int}) \leq -38.0 + 1.72\log(N_{H_2}^{beam}), \text{ and } \log(N_{H_2}^{beam}) \geq 22.1, \quad (4)$$

We can then extrapolate the identified class I methanol maser region to the full BGPS sample to estimate the likely number of class I methanol masers. The distribution of all BGPS sources with the class I maser region overlaid is present in the right panel of Figure 13. In total, approximate 1200 sources are located within the defined class I maser region. If we extrapolate the results of this study we would predict that we can detect 90% of all the expected (~ 1000 ; see Table 7) class I methanol masers associated with BGPS sources and that the detection efficiency would be about 75% towards the sources within the defined region. Since the above estimates are based on all 95 GHz detections (including possible thermal sources), the number of real maser source detections may be at 80% (at worst) of the above predictions (see discussion above).

However, a search for class I methanol maser towards an unbiased sample of BGPS sources is required to clarify all possible sample selection effects and to reliably estimate the true number of methanol masers associated with the full BGPS catalog. Since the BGPS only covers around half of the inner Galaxy, the total number of class I methanol masers

in the Galaxy would be expected to be at least double the number associated with BGPS sources, suggesting that class I methanol masers may be significantly more numerous in the Galaxy than are class II methanol masers.

5. Summary

Using the PMO 13.7-m radio telescope, we have performed a search for 95 GHz class I methanol masers toward a sample selected from a combination of the mid-IR *spitzer* GLIMPSE and 1.1 mm CSO BGPS surveys. A total of 214 sources were selected as the observing sample, and these satisfy the GLIMPSE mid-IR criteria of $[3.6]-[4.5]>1.3$, $[3.6]-[5.8]>2.5$, $[3.6]-[8.0]>2.5$ and $8.0 \mu\text{m}$ magnitude less than 10, and are also associated with a 1.1 mm BGPS source. 95 GHz class I methanol maser emission was detected toward 63 sources, of these 51 are new 95 GHz class I methanol maser sources, and 43 have no previously observed class I methanol maser activity. Thus a detection rate of $\sim 29\%$ was observed for class I methanol masers in the conjunct sample of GLIMPSE and BGPS surveys from our single-dish survey. We also find that the sensitivity of survey exceeds the theoretical detection limit derived from the observed dependence between the integrated class I maser emission and the BGPS beam-averaged column density.

Analysis of the mid-IR colors of GLIMPSE point sources in our observing sample indicates that the color-color region occupied by those sources with and without an associated class I methanol maser are not significantly different. However, the detection rate of class I methanol masers is higher towards those GLIMPSE point sources with redder mid-IR colors. The mid-IR characteristics the GLIMPSE sources associated with class I methanol masers in the current sample is very similar to that derived in our earlier EGO-selected sample. We find that the class I methanol maser intensity is not closely related to either the mid-IR emission intensity nor the color of the associated GLIMPSE point sources. However, the maser emission is well correlated with the gas mass derived for the BGPS sources. Comparison of the properties of BGPS sources with and without an associated methanol maser shows that those with an associated class I methanol maser usually have higher beam-averaged H_2 column density and larger BGPS flux density than those without an associated maser.

A series of investigations of the detection rates of class I methanol masers as a function of GLIMPSE mid-IR and BGPS properties were undertaken, with the aim of developing more efficient criteria for future targeted class I methanol maser searches. Although the detection rates of class I methanol masers appear to some extent to be dependent on the mid-IR properties of GLIMPSE point sources (such as $4.5 \mu\text{m}$ magnitude and $[3.6]-[4.5]$ color), tighter correlations are observed between the class I methanol maser detection rate and the BGPS

source properties. This suggests that the BGPS catalog could provide much more efficient target samples for future class I methanol maser searches. Based on the observed relationship between the detection rate of class I methanol maser and the BGPS beam-averaged H_2 column density, we estimate that approximately 1000 (of ~ 8400) BGPS sources may have an associated class I methanol maser. We identify a region in the distribution of BGPS beam-average column density versus BGPS integrated flux density (satisfying $\log(S_{int}) \leq -38.0 + 1.72\log(N_{H_2}^{beam})$, and $\log(N_{H_2}^{beam}) \geq 22.1$), towards which we expect to find 90% of all (~ 1000) class I methanol masers with a high detection efficiency ($\sim 75\%$).

We thank an anonymous referee for their helpful comments which have improved this paper. We are grateful to the staff of Qinghai Station of Purple Mountain Observatory for their assistance in the observation. This research has made use of the data products from the GLIMPSE survey, which is a legacy science program of the *Spitzer Space Telescope* funded by the National Aeronautics and Space Administration, and made use of information from the BGPS survey database at http://irsa.ipac.caltech.edu/data/BOLOCAM_GPS/. This work is partly supported by China Ministry of Science and Technology under State Key Development Program for Basic Research (2012CB821800), the National Natural Science Foundation of China (grants 10621303, 10625314, 10803017, 10821302, 11073041, 11073054, 11133008, 11173046), the CAS/SAFEA International Partnership Program for Creative Research Teams, and Key Laboratory for Radio Astronomy, CAS. .

REFERENCES

- Aguirre, J. E., Ginsburg, A. G., Dunham, M. K., et al. 2011, *ApJS*, 192, 4
- Bae, J. H., Kim, K. T., Youn, S. Y., Kim, W. J., Byun, D. Y., Kang, H., & Oh, C. S. 2001, *ApJS*, 196, 21
- Batrla, W., & Menten, K. M. 1988, *ApJ*, 329, L117
- Benjamin, R. A., Churchwell, E., Babler, B. L., et al. 2003, *PASP*, 115, 953
- Breen, S. L., Ellingsen, S. P., Johnston-Hollitt, M., et al. 2007, *MNRAS*, 377, 491
- Breen, S. L., & Ellingsen, S. P. 2011, *MNRAS*, 416, 178
- Carey, S. J., Clark, F. O., Egan, M. P., et al. 1998, *ApJ*, 508, 721
- Carey, S. J., Feldman, P. A., Redman, R. O., et al. 2000, *ApJ*, 543, L157

- Caswell, J. L. 2009, PASA, 26, 454
- Caswell, J. L., et al. 2010, MNRAS, 404, 1029
- 2011, MNRAS, 417, 1964
- Chambers, E. T., Yusef-Zadeh, F., & Roberts, D. 2011, ApJ, 733, 42
- Chen, X., Ellingsen, S. P., & Shen, Z. Q. 2009, MNRAS, 396, 1603
- Chen, X., Ellingsen, S. P., Shen, Z. Q., Titmarsh, A., & Gan, C. G. 2011, ApJS, 196, 9
- Churchwell, E., et al. 2009, PASP, 121, 213
- Cragg, D. M., Johns, K. P., Godfrey, P. D., & Brown, R. D. 1992, MNRAS, 259, 203
- Cyganowski, C. J., Brogan, C. L., Hunter, T. R., & Churchwell, E. 2009, ApJ, 702, 1615
- Cyganowski, C. J., Whitney, B. A., Holden, E., et al. 2008, AJ, 136, 2391
- Dunham, M. K., Rosolowsky, E., Evans, N. J., II., et al. 2010, ApJ, 717, 1157
- Dunham, M. K., Robitaille, T. P., Evans, N. J., II., et al. 2011a, ApJ, 731, 90
- Dunham, M. K., Rosolowsky, E., Evans, N. J., II., et al., 2011b ApJ, in press
- Egan, M. P., Shipman, R. F., Price, S. D., et al. 1998, ApJ, 494, L199
- Ellingsen, S. P. 2005, MNRAS, 359, 1498
- Ellingsen, S. P. 2006, ApJ, 638, 241
- Ellingsen, S. P. 2007, MNRAS, 377, 571
- Fish, V. L., Muehlbrad, T. C., Pratap, P., Sjouwerman, L. O., Strel'nitski, V., Pihlström, Y. M., & Bourke, T. L. 2011, ApJ, 729, 14
- Fontani, F., Cesaroni, R., & Furuya, R. S., 2010, A&A, 517, 56
- Glenn, J., Ade, P. A. R., Amarie, M., et al. 2003, Proc. SPIE, 4855, 30
- Goedhart, S., Gaylard, M. J., & van der Walt, D. J. 2004, MNRAS, 355, 553
- Goedhart, S., Langa, M. C., Gaylard, M. J., & van der Walt, D. J. 2009, MNRAS, 398, 995
- Green, J. A., et al. 2009, MNRAS, 392, 783

— 2010, MNRAS, 409, 913

— 2012, in press

Green, J. A., & McClure-Griffiths, N. M. 2011, MNRAS, 417, 2500

Haig, D. J., Ade, P. A. R., Aguirre, J., et al. 2004, Proc. SPIE, 5498, 78

Haschick, A. D., Menten, K. M., & Baan, W. A. 1990, ApJ, 354, 556

Heiderman, A., Evans, N. J. II., Allen, L. E., Huard, T., & Heyer, M. 2010, ApJ, 723, 1019

Hoare, M. G., Lumsden, S. L., Oudmaijer, R. D., et al. 2004, in ASP Conf. Ser. 317, Milky Way Surveys: The Structure and Evolution of Our Galaxy, ed. D. Clemens, R. Shah, & T. Brainerd (San Francisco, CA: ASP), 156

Indebetouw, R., et al. 2005, ApJ, 619, 931

Jackson, J. M., Finn, S. C., Rathborne, J. M., Chambers, E. T., & Simon, R. 2008, ApJ, 680, 349

Kalenskii, S. V., Johansson, L. E. B., Bergman, P., Kurtz, S., Hofner, P., Walmsley, C. M., & Slysh, V. I. 2010, MNRAS, 405, 613

Kurtz, S., Hofner, P., & Álvarez, C. V. 2004, ApJS, 155, 149

Lada, C. J., Lombardi, M., & Alves, J. F. 2010, ApJ, 724, 687

Menten K. M. 1991, in “Skylines” proceedings of the Third Haystack Observatory Meeting, ed. A. D. Haschick, P. T. P. Ho (San Fransisco: Astronomical Society of the Pacific), 119

Müller, H. S. P., Menten, K. M., & Mäder, H. 2004, A&A, 428, 1019

Ossenkopf, V., & Henning, T. 1994, A&A, 291, 943

Pandian, J. D., Goldsmith, P. F., & Deshpande, A. A. 2007, ApJ, 656, 255

Peretto, N., & Fuller, G. A. 2009, A&A, 505, 405

Pestalozzi, M. R., Minier, V., & Booth, R. S. 2005, A&A, 432, 737

Pihlström, Y. M., Sjouwerman, L. O., & Fish, V. L. 2011, ApJ, 739, L21

Plambeck, R. L., & Menten, K. M. 1990, ApJ, 364, 555

- Povich, M. S., & Whitney, B. A. 2010, *ApJ*, 714, 285
- Povich, M. S., Churchwell, E., Bieging, J. H., et al. 2009, *ApJ*, 696, 1278
- Pratap, P., Strel'nitski, V., Hoffman, S., & Lemonias, J. 2007, *IAU Symp. 242, Astrophysical Masers and their Environments*, ed. J. M. Chapman & W. A. Baan (Cambridge: Cambridge Univ. Press), 34
- Reid, M. J., et al. 2009, *ApJ*, 700, 137
- Robitaille, T. P., Whitney, B. A., Indebetouw, R., Wood, K., & Denzmore, P. 2006, *ApJS*, 167, 256
- Robitaille, T. P., et al. 2008, *AJ*, 136, 2413
- Rosolowsky, E., et al. 2010, *ApJS*, 188, 123
- Sarma, A. P., & Momjian, E. 2009, *ApJ*, 705, L176
- 2011, *ApJ*, 730, L5
- Schlingman, W. M., Shirley, Y. L., Schenk, D. E., et al. 2011, *ApJS*, 195, 14
- Simon, R., Jackson, J. M., Rathborne, J. M., & Chambers, E. T. 2006a, *ApJ*, 639, 227
- Simon, R., Rathborne, J. M., Shah, R. Y., Jackson, J. M., & Chambers, E. T. 2006b, *ApJ*, 653, 1325
- Slysh, V. I., Kalenskii, S. V., Val'tts, I. E., & Otrupcek, R. 1994, *MNRAS*, 268, 464
- Szymczak, M., Wolak, P., Bartkiewicz, A., & van Langevelde, H. J. 2011, *A&A*, 531, 3L
- Urquhart, J. S., Busfield, A. L., Hoare, M. G., et al. 2009, *A&A*, 487, 253
- Val'tts, I. E., Ellingsen, S. P., Slysh, V. I., Kalenskii, S. V., Otrupcek, R., & Larinov, G. M. 2000, *MNRAS*, 317, 315
- Voronkov, M. A., Brooks, K. J., Sobolev, A. M., Ellingsen, S. P., Ostrovskii, A. B., & Caswell J. L. 2006, *MNRAS*, 373, 411
- Voronkov, M. A., Caswell, J. L., Ellingsen, S. P., & Sobolev, A. M. 2010a, *MNRAS*, 405, 2471
- 2010b, *MNRAS*, 405, 2471

Voronkov, M. A., Sobolev, A. M., Ellingsen, S. P., & Ostrovskii, A. B. 2005, MNRAS, 362, 995

Voronkov, M. A., Walsh, A. J., Caswell, J. L., et al. 2011, MNRAS, 413, 2339

Xu, Y., Li, J. J., Hachisuka, K., Pandian, J. D., Menten, K. M., & Henkel, C. 2008, A&A, 485, 729

Xu, Y., Voronkov, M. A., Pandian, J. D., Li, J. J., Sobolev, A. M., Brunthaler, A., Ritter, B., & Menten, K. M. 2009, A&A, 507, 1117

Table 1—Continued

| Number | GLIMPSE Point Source | | | | | BGPS Source | | | | | $N_{H_2}^{beam}$ (10^{22} cm $^{-2}$) |
|--------|----------------------|----------------------|----------------------|----------------------|----------------------|-------------|-----------------|---------------|---------------------|--------------------|--|
| | Name | 3.6 μ m (mag) | 4.5 μ m (mag) | 5.8 μ m (mag) | 8.0 μ m (mag) | ID | Name | R ($''$) | S $_{40''}$ (Jy) | S $_{int}$ (Jy) | |
| (1) | (2) | (3) | (4) | (5) | (6) | (7) | (8) | (9) | (10) | (11) | (12) |
| 129 | G029.3199-00.1615 | 11.16(0.12) | 8.54(0.07) | 7.11(0.03) | 6.37(0.03) | 4139 | G029.318-00.165 | 21.24 | 0.156(0.040) | 0.338(0.076) | 0.94 |
| 130 | G029.7801-00.2594 | 12.46(0.08) | 10.43(0.08) | 9.38(0.08) | 8.66(0.09) | 4219 | G029.781-00.262 | 45.50 | 0.224(0.036) | 0.910(0.115) | 1.35 |
| 131 | G030.0100+00.0356 | 12.04(0.06) | 9.99(0.06) | 8.15(0.03) | 7.03(0.03) | 4284 | G030.010+00.034 | - | 0.127(0.044) | 0.304(0.084) | 0.77 |
| 132 | G030.2116-00.1885 | 14.20(0.22) | 11.35(0.10) | 9.50(0.10) | 8.69(0.24) | 4321 | G030.215-00.188 | 83.95 | 0.917(0.070) | 5.916(0.407) | 5.53 |
| 133 | G030.3476+00.3917 | 10.75(0.10) | 8.27(0.09) | 7.05(0.04) | 6.69(0.04) | 4366 | G030.347+00.390 | 77.98 | 0.387(0.039) | 1.973(0.178) | 2.33 |
| 134 | G030.4204-00.2283 | 12.66(0.15) | 10.36(0.30) | 9.01(0.06) | 8.29(0.08) | 4398 | G030.419-00.232 | 87.20 | 1.500(0.102) | 7.704(0.522) | 9.04 |
| 135 | G030.6039+00.1760 | 12.43(0.06) | 9.07(0.18) | 7.14(0.03) | 6.92(0.03) | 4472 | G030.603+00.175 | 128.72 | 1.462(0.098) | 12.965(0.830) | 8.81 |
| 136 | G030.6622-00.1393 | 13.47(0.13) | 11.22(0.09) | 9.74(0.11) | 9.12(0.17) | 4492 | G030.666-00.139 | 53.89 | 0.298(0.034) | 1.316(0.123) | 1.80 |
| 137 | G030.6670-00.3318 | 9.72(0.18) | 7.42(0.08) | 6.12(0.02) | 4.09(0.03) | 4497 | G030.667-00.331 | - | 0.116(0.027) | 0.192(0.044) | 0.70 |
| 138 | G030.8107+00.1895 | 14.58(0.13) | 12.43(0.08) | 10.90(0.08) | 9.94(0.08) | 4556 | G030.812+00.191 | 47.60 | 0.225(0.035) | 0.841(0.093) | 1.36 |
| 139 | G030.8685-00.1188 | 14.42(0.33) | 12.13(0.24) | 10.57(0.15) | 9.52(0.26) | 4581 | G030.868-00.121 | 73.45 | 0.420(0.040) | 3.184(0.226) | 2.53 |
| 140 | G030.9447+00.1574 | 11.54(0.07) | 9.34(0.05) | 8.19(0.03) | 7.37(0.03) | 4621 | G030.948+00.159 | 28.30 | 0.125(0.032) | 0.351(0.066) | 0.75 |
| 141 | G030.9588+00.0863 | 9.05(0.19) | 6.89(0.07) | 5.26(0.04) | 4.58(0.13) | 4627 | G030.960+00.085 | 54.60 | 0.600(0.046) | 2.191(0.166) | 3.62 |
| 142 | G030.9949+00.2339 | 14.15(0.13) | 11.55(0.10) | 10.43(0.06) | 9.89(0.07) | 4642 | G030.998+00.235 | 63.53 | 0.378(0.037) | 2.153(0.163) | 2.28 |
| 143 | G031.0147+00.7783 | 14.52(0.12) | 11.59(0.10) | 8.62(0.05) | 7.06(0.10) | 4649 | G031.013+00.781 | - | 0.140(0.068) | 0.184(0.076) | 0.84 |
| 144 | G031.0738+00.4596 | 13.79(0.08) | 11.44(0.08) | 10.22(0.05) | 9.93(0.05) | 4673 | G031.077+00.459 | 66.76 | 0.417(0.040) | 2.136(0.173) | 2.51 |
| 145 | G031.1016+00.2644 | 13.93(0.12) | 11.16(0.08) | 9.72(0.07) | 9.21(0.12) | 4678 | G031.103+00.265 | 64.32 | 0.184(0.029) | 1.178(0.121) | 1.11 |
| 146 | G031.1825-00.1479 | 13.04(0.09) | 10.75(0.07) | 9.43(0.05) | 8.38(0.05) | 4701 | G031.182-00.145 | 73.20 | 0.289(0.034) | 1.824(0.154) | 1.74 |
| 147 | G031.3911+00.2037 | 12.47(0.10) | 10.41(0.13) | 8.68(0.05) | 7.60(0.07) | 4759 | G031.394+00.207 | 87.18 | 0.207(0.032) | 1.407(0.146) | 1.25 |
| 148 | G031.5813+00.0788 | 13.31(0.14) | 11.12(0.09) | 9.15(0.05) | 7.40(0.04) | 4812 | G031.582+00.077 | 73.18 | 1.053(0.072) | 3.928(0.278) | 6.35 |
| 149 | G031.9003+00.3410 | 13.03(0.09) | 10.85(0.08) | 10.39(0.06) | 9.90(0.07) | 4892 | G031.900+00.343 | 53.48 | 0.164(0.028) | 0.679(0.088) | 0.99 |
| 150 | G032.6058-00.2557 | 14.51(0.22) | 11.69(0.11) | 9.66(0.06) | 8.77(0.07) | 5008 | G032.605-00.253 | 88.71 | 0.207(0.027) | 1.963(0.163) | 1.25 |
| 151 | G032.7038-00.0560 | 12.25(0.23) | 9.48(0.14) | 8.25(0.06) | 7.59(0.12) | 5032 | G032.704-00.059 | 46.07 | 0.333(0.034) | 1.151(0.107) | 2.01 |
| 152 | G032.8264-00.0824 | 12.66(0.20) | 10.22(0.06) | 9.26(0.06) | 8.87(0.06) | 5061 | G032.829-00.081 | 71.84 | 0.227(0.029) | 1.147(0.119) | 1.37 |
| 153 | G032.9917+00.0339 | 10.59(0.06) | 8.55(0.13) | 7.40(0.04) | 6.93(0.04) | 5100 | G032.991+00.037 | 75.21 | 0.759(0.055) | 3.401(0.249) | 4.57 |
| 154 | G033.3928+00.0097 | 10.69(0.08) | 7.62(0.04) | 6.55(0.03) | 5.95(0.03) | 5167 | G033.390+00.008 | 98.64 | 0.813(0.063) | 6.914(0.471) | 4.90 |
| 155 | G033.4007+00.3713 | 13.50(0.13) | 11.38(0.07) | 9.86(0.06) | 8.69(0.06) | 5170 | G033.404+00.370 | - | 0.068(0.026) | 0.194(0.048) | 0.41 |
| 156 | G033.6754+00.2031 | 14.49(0.14) | 12.34(0.11) | 10.83(0.07) | 9.92(0.04) | 5230 | G033.672+00.201 | 65.65 | 0.144(0.033) | 0.799(0.116) | 0.87 |
| 157 | G033.7042+00.2821 | 14.10(0.12) | 11.12(0.09) | 10.40(0.05) | 9.74(0.07) | 5240 | G033.704+00.285 | 40.95 | 0.269(0.036) | 0.963(0.105) | 1.62 |
| 158 | G033.7395-00.0198 | 13.87(0.19) | 11.48(0.12) | 9.71(0.04) | 8.06(0.02) | 5252 | G033.740-00.017 | 90.78 | 0.708(0.062) | 5.136(0.375) | 4.27 |
| 159 | G033.8181-00.2121 | 11.26(0.11) | 9.24(0.06) | 8.65(0.03) | 8.24(0.03) | 5265 | G033.817-00.215 | 29.71 | 0.152(0.037) | 0.430(0.077) | 0.92 |
| 160 | G033.8519+00.0180 | 13.54(0.10) | 10.70(0.12) | 9.38(0.04) | 9.25(0.04) | 5270 | G033.850+00.017 | 64.54 | 0.260(0.032) | 1.111(0.121) | 1.57 |
| 161 | G034.4119+00.2343 | 14.15(0.20) | 11.36(0.17) | 10.55(0.12) | 9.99(0.12) | 5373 | G034.410+00.232 | 96.10 | 3.337(0.210) | 20.777(1.303) | 20.11 |
| 162 | G034.9333+00.0194 | 13.99(0.19) | 11.76(0.08) | 9.25(0.04) | 7.79(0.04) | 5501 | G034.932+00.022 | 71.21 | 0.254(0.037) | 1.292(0.147) | 1.53 |
| 163 | G034.9941-00.0446 | 12.11(0.10) | 9.62(0.10) | 8.46(0.04) | 7.77(0.04) | 5516 | G034.991-00.046 | 46.34 | 0.163(0.037) | 0.689(0.104) | 0.98 |
| 164 | G035.2252-00.3596 | 11.47(0.06) | 9.33(0.05) | 8.04(0.04) | 7.10(0.03) | 5572 | G035.228-00.358 | 22.89 | 0.364(0.043) | 0.784(0.095) | 2.19 |
| 165 | G035.2474-00.2368 | 11.77(0.19) | 9.37(0.10) | 8.74(0.04) | 7.78(0.03) | 5577 | G035.247-00.238 | - | 0.087(0.038) | 0.123(0.047) | 0.52 |
| 166 | G035.3145-00.2254 | 12.16(0.12) | 10.10(0.09) | 9.15(0.04) | 8.12(0.03) | 5594 | G035.316-00.222 | 58.23 | 0.149(0.036) | 0.673(0.111) | 0.90 |
| 167 | G035.7095+00.1631 | 12.84(0.13) | 10.49(0.07) | 9.39(0.04) | 8.82(0.04) | 5691 | G035.707+00.164 | - | 0.065(0.032) | 0.084(0.036) | 0.39 |
| 168 | G036.0011-00.4644 | 13.50(0.13) | 11.43(0.08) | 10.00(0.05) | 8.99(0.03) | 5720 | G035.997-00.466 | 79.56 | 0.163(0.034) | 1.266(0.146) | 0.98 |
| 169 | G036.0127-00.1974 | 13.03(0.19) | 9.70(0.14) | 9.66(0.07) | 9.57(0.04) | 5722 | G036.012-00.198 | 36.14 | 0.242(0.037) | 0.674(0.094) | 1.46 |
| 170 | G036.7053+00.0962 | 10.75(0.08) | 8.70(0.07) | 8.09(0.04) | 7.70(0.03) | 5782 | G036.704+00.094 | 70.92 | 0.156(0.037) | 1.088(0.147) | 0.94 |
| 171 | G037.3418-00.0591 | 9.93(0.11) | 7.63(0.07) | 5.75(0.03) | 4.68(0.05) | 5836 | G037.341-00.062 | 79.89 | 0.445(0.045) | 2.281(0.204) | 2.68 |
| 172 | G037.7632-00.2150 | 10.15(0.06) | 7.99(0.04) | 6.85(0.04) | 6.34(0.06) | 5869 | G037.765-00.216 | 50.07 | 1.262(0.093) | 4.569(0.331) | 7.61 |
| 173 | G038.1616-00.0747 | 13.82(0.08) | 11.79(0.09) | 10.44(0.07) | 9.98(0.11) | 5896 | G038.161-00.078 | 33.10 | 0.151(0.049) | 0.426(0.102) | 0.91 |
| 174 | G038.5548+00.1624 | 10.55(0.09) | 8.53(0.09) | 7.28(0.04) | 6.83(0.09) | 5919 | G038.552+00.160 | - | 0.261(0.047) | 0.582(0.095) | 1.57 |
| 175 | G038.5977-00.2125 | 12.19(0.07) | 9.88(0.07) | 8.79(0.04) | 8.05(0.03) | 5922 | G038.599-00.214 | 53.12 | 0.196(0.041) | 0.821(0.124) | 1.18 |
| 176 | G038.8471-00.4295 | 13.18(0.06) | 10.88(0.06) | 9.65(0.05) | 8.66(0.05) | 5941 | G038.847-00.428 | 85.04 | 0.246(0.037) | 1.435(0.159) | 1.48 |
| 177 | G039.5875-00.2064 | 13.33(0.08) | 11.27(0.06) | 10.26(0.05) | 9.76(0.10) | 5993 | G039.591-00.205 | 60.24 | 0.190(0.043) | 1.069(0.149) | 1.15 |
| 178 | G040.1579+00.1686 | 8.71(0.15) | 7.41(0.14) | 6.04(0.05) | 4.90(0.10) | 6017 | G040.157+00.167 | - | 0.111(0.039) | 0.220(0.063) | 0.67 |
| 179 | G040.2782-00.2691 | 10.58(0.13) | 8.43(0.09) | 7.35(0.03) | 6.69(0.03) | 6023 | G040.279-00.269 | 31.00 | 0.187(0.044) | 0.458(0.092) | 1.13 |
| 180 | G041.8828+00.4689 | 14.57(0.23) | 12.46(0.11) | 10.39(0.06) | 9.08(0.06) | 6086 | G041.883+00.469 | - | 0.116(0.047) | 0.265(0.081) | 0.70 |
| 181 | G043.0386-00.4535 | 13.10(0.09) | 10.89(0.09) | 9.95(0.07) | 9.13(0.06) | 6110 | G043.039-00.455 | 27.60 | 0.794(0.074) | 1.706(0.168) | 4.79 |
| 182 | G043.0757-00.0781 | 12.21(0.06) | 10.59(0.04) | 9.56(0.04) | 8.90(0.04) | 6111 | G043.073-00.079 | 31.59 | 0.237(0.061) | 0.614(0.128) | 1.43 |
| 183 | G043.9293-00.3352 | 13.46(0.12) | 10.92(0.10) | 9.78(0.06) | 8.85(0.05) | 6131 | G043.929-00.335 | 14.35 | 0.114(0.043) | 0.231(0.071) | 0.69 |
| 184 | G044.0967+00.1601 | 11.97(0.07) | 9.70(0.06) | 8.60(0.04) | 7.82(0.03) | 6137 | G044.099+00.163 | 20.12 | 0.141(0.048) | 0.377(0.093) | 0.85 |
| 185 | G044.5215+00.3902 | 10.69(0.07) | 9.10(0.06) | 7.60(0.03) | 6.39(0.04) | 6153 | G044.521+00.387 | 23.84 | 0.221(0.049) | 0.551(0.101) | 1.33 |
| 186 | G045.1669+00.0911 | 11.89(0.15) | 9.29(0.07) | 7.81(0.04) | 6.64(0.03) | 6166 | G045.167+00.095 | 39.35 | 0.189(0.053) | 0.654(0.127) | 1.14 |
| 187 | G045.5683-00.1201 | 11.70(0.16) | 9.34(0.10) | 8.06(0.04) | 7.78(0.10) | 6188 | G045.569-00.119 | 27.91 | 0.121(0.036) | 0.315(0.073) | 0.73 |
| 188 | G045.8818-00.5095 | 11.69(0.06) | 9.73(0.05) | 8.69(0.04) | 7.86(0.03) | 6208 | G045.884-00.509 | - | 0.196(0.050) | 0.480(0.093) | 1.18 |
| 189 | G046.3163-00.2109 | 13.00(0.08) | 11.04(0.07) | 9.99(0.07) | 9.54(0.07) | 6225 | G046.314-00.213 | 30.28 | 0.129(0.039) | 0.407(0.085) | 0.78 |
| 190 | G048.6113+00.2211 | 12.01(0.07) | 10.06(0.05) | 8.91(0.04) | 8.16(0.04) | 6258 | G048.609+00.220 | - | 0.126(0.057) | 0.240(0.081) | 0.76 |
| 191 | G048.8398-00.4837 | 13.88(0.07) | 12.21(0.10) | 11.04(0.10) | 9.99(0.07) | 6280 | G048.841-00.482 | 59.75 | 0.203(0.055) | 0.833(0.158) | 1.22 |
| 192 | G049.0721-00.3270 | 10.22(0.14) | 8.31(0.09) | 6.91(0.03) | 6.08(0.03) | 6298 | G049.069-00.328 | 63.88 | 0.660(0.079) | 3.313(0.317) | 3.98 |

Table 1—Continued

| Number | GLIMPSE Point Source | | | | BGPS Source | | | | | | |
|--------|----------------------|-------------------|-------------------|-------------------|-------------------|------|-----------------|--------|-------------------|------------------|--|
| | Name | 3.6 μm | 4.5 μm | 5.8 μm | 8.0 μm | ID | Name | R | S _{40''} | S _{int} | N _{H₂} ^{beam} |
| (1) | (2) | (mag) | (mag) | (mag) | (mag) | (7) | (8) | ('') | (Jy) | (Jy) | (10 ²² cm ⁻²) |
| | | (3) | (4) | (5) | (6) | | | (9) | (10) | (11) | (12) |
| 193 | G049.1073–00.2681 | 13.31(0.22) | 11.82(0.08) | 10.6(0.14) | 9.99(0.20) | 6304 | G049.106–00.272 | 28.96 | 0.189(0.054) | 0.625(0.108) | 1.14 |
| 194 | G049.2634–00.3401 | 12.40(0.06) | 10.29(0.09) | 9.28(0.06) | 8.51(0.06) | 6323 | G049.267–00.338 | 51.77 | 1.662(0.120) | 6.088(0.437) | 10.02 |
| 195 | G049.3811–00.1840 | 12.26(0.09) | 10.59(0.12) | 9.28(0.05) | 8.33(0.04) | 6338 | G049.378–00.184 | 28.03 | 0.212(0.051) | 0.478(0.101) | 1.28 |
| 196 | G049.4065–00.3715 | 12.14(0.11) | 9.69(0.07) | 7.97(0.05) | 6.92(0.07) | 6346 | G049.405–00.370 | 54.92 | 0.729(0.117) | 3.622(0.401) | 4.39 |
| 197 | G049.6006–00.2468 | 13.59(0.09) | 11.94(0.10) | 9.35(0.06) | 7.74(0.10) | 6376 | G049.599–00.250 | 24.03 | 0.362(0.062) | 0.862(0.134) | 2.18 |
| 198 | G049.8149+00.4540 | 14.05(0.13) | 11.80(0.07) | 10.74(0.08) | 9.99(0.07) | 6380 | G049.817+00.456 | – | 0.109(0.061) | 0.226(0.091) | 0.66 |
| 199 | G050.0644+00.0633 | 13.24(0.06) | 11.38(0.07) | 9.98(0.06) | 9.21(0.06) | 6387 | G050.060+00.062 | 64.17 | 0.359(0.071) | 2.279(0.265) | 2.16 |
| 200 | G053.1398+00.0707 | 8.88(0.20) | 7.49(0.16) | 6.19(0.05) | 4.97(0.04) | 6414 | G053.142+00.068 | 58.07 | 1.477(0.118) | 5.605(0.445) | 8.90 |
| 201 | G053.1632–00.2455 | 13.40(0.11) | 10.29(0.07) | 8.65(0.06) | 8.17(0.17) | 6416 | G053.164–00.246 | 38.57 | 0.468(0.066) | 1.272(0.171) | 2.82 |
| 202 | G053.2480–00.0869 | 12.13(0.06) | 9.87(0.05) | 8.74(0.03) | 7.86(0.04) | 6424 | G053.248–00.086 | – | 0.127(0.057) | 0.288(0.096) | 0.77 |
| 203 | G053.4552+00.0044 | 13.58(0.12) | 12.27(0.15) | 10.92(0.16) | 9.38(0.15) | 6429 | G053.457+00.004 | 36.56 | 0.155(0.069) | 0.516(0.147) | 0.93 |
| 204 | G053.6180+00.0352 | 10.01(0.21) | 7.38(0.16) | 5.69(0.03) | 4.94(0.03) | 6433 | G053.616+00.036 | 41.16 | 0.618(0.086) | 1.894(0.239) | 3.72 |
| 205 | G053.6316+00.0134 | 12.78(0.06) | 11.02(0.08) | 9.63(0.06) | 8.52(0.04) | 6437 | G053.634+00.014 | 39.82 | 0.245(0.075) | 0.886(0.182) | 1.48 |
| 206 | G053.9436–00.0774 | 10.88(0.04) | 9.26(0.04) | 8.03(0.03) | 7.16(0.04) | 6445 | G053.942–00.080 | 19.49 | 0.091(0.060) | 0.264(0.102) | 0.55 |
| 207 | G054.1098–00.0813 | 9.26(0.07) | 7.90(0.07) | 6.58(0.03) | 5.58(0.03) | 6451 | G054.112–00.083 | 113.32 | 0.712(0.097) | 6.994(0.586) | 4.29 |
| 208 | G054.3890–00.0335 | 10.15(0.09) | 8.61(0.05) | 7.35(0.02) | 6.42(0.04) | 6455 | G054.390–00.035 | 31.23 | 0.225(0.070) | 0.664(0.149) | 1.36 |
| 209 | G056.9631–00.2346 | 9.49(0.17) | 7.69(0.09) | 6.63(0.04) | 6.08(0.10) | 6470 | G056.962–00.234 | 25.81 | 0.243(0.090) | 0.630(0.170) | 1.46 |
| 210 | G058.4719+00.4340 | 11.16(0.05) | 9.54(0.05) | 8.40(0.04) | 7.67(0.03) | 6474 | G058.471+00.433 | 22.51 | 0.400(0.000) | 0.914(0.212) | 2.41 |
| 211 | G059.4978–00.2365 | 10.97(0.07) | 8.48(0.06) | 6.84(0.03) | 5.56(0.03) | 6476 | G059.499–00.235 | 42.20 | 0.399(0.076) | 1.374(0.202) | 2.40 |
| 212 | G059.6366–00.1864 | 11.48(0.11) | 9.57(0.11) | 8.79(0.06) | 8.33(0.08) | 6479 | G059.639–00.189 | 39.85 | 1.531(0.130) | 4.660(0.391) | 9.23 |
| 213 | G060.0162+00.1115 | 12.58(0.13) | 10.42(0.14) | 9.49(0.06) | 8.23(0.08) | 6492 | G060.017+00.115 | 27.06 | 0.407(0.088) | 1.010(0.172) | 2.45 |
| 214 | G063.0768+00.1853 | 11.63(0.14) | 9.41(0.07) | 8.13(0.04) | 6.91(0.03) | 6501 | G063.075+00.184 | – | 0.185(0.080) | 0.200(0.102) | 1.11 |

Note. — Column (1): source number which is organized by increasing galactic longitude. Column (2): GLIMPSE point source name. Columns (3) – (6): the magnitude of the GLIMPSE point source in the 3.6, 4.5, 5.8 and 8.0 μm bands, respectively. Columns (7) and (8): the ID number and name of BGPS source, respectively. Column (9): the radius of BGPS, sources which are unresolved with the BGPS beam, are indicated with “–” in this column. Columns (10) and (11): the aperture flux density within 40'' and the integrated flux density of the BGPS sources. Note that a flux calibration correction factor of 1.5 should be applied to the both the aperture and integrated flux densities listed here to calculate BGPS gas mass and column/volume density (see Section 4.2). In addition, an aperture correction of 1.46 is needed to apply to aperture flux density within 40'' after applied a flux calibration correction factor of 1.5 to calculate the beam-averaged column density. Columns (12): the beam-averaged H₂ column density (see section 4.2).

Table 2. Observed source positions and observing rms noise.

| Number | BGPS ID | R.A. (J2000) | Decl. (J2000) | σ_{rms} (Jy) | Number | BGPS ID | R.A. (J2000) | Decl. (J2000) | σ_{rms} (Jy) |
|--------|---------|--------------|---------------|---------------------|--------|---------|--------------|---------------|---------------------|
| 1 | 1051 | 17 56 25.86 | -24 48 17.0 | 0.9 | 108 | 3530 | 18 38 35.11 | -06 41 27.1 | 1.2 |
| 2 | 1053 | 17 55 54.71 | -24 42 46.7 | 0.9 | 109 | 3699 | 18 39 56.20 | -05 38 48.3 | 0.9 |
| 3 | 1066 | 17 56 49.37 | -24 38 37.0 | 1.1 | 110 | 3721 | 18 38 57.67 | -05 14 41.2 | 1.0 |
| 4 | 1071 | 17 57 32.79 | -24 39 03.9 | 0.9 | 111 | 3741 | 18 39 54.38 | -05 10 05.3 | 0.4 |
| 5 | 1084 | 17 58 09.70 | -24 23 49.2 | 0.5 | 112 | 3771 | 18 40 39.47 | -05 00 21.0 | 0.9 |
| 6 | 1087 | 17 57 48.30 | -24 19 03.8 | 0.9 | 113 | 3822 | 18 41 20.84 | -04 32 20.6 | 1.0 |
| 7 | 1090 | 17 56 41.11 | -24 09 21.4 | 1.0 | 114 | 3833 | 18 42 56.88 | -04 41 57.6 | 1.0 |
| 8 | 1131 | 18 00 21.60 | -24 05 56.6 | 0.9 | 115 | 3863 | 18 43 52.92 | -04 36 19.3 | 1.1 |
| 9 | 1164 | 17 59 30.07 | -23 44 15.4 | 0.9 | 116 | 3876 | 18 44 09.20 | -04 33 24.9 | 1.0 |
| 10 | 1203 | 18 00 17.92 | -23 26 20.2 | 1.0 | 117 | 3897 | 18 42 43.01 | -04 15 37.5 | 0.8 |
| 11 | 1251 | 18 02 12.80 | -23 05 44.4 | 1.0 | 118 | 3917 | 18 41 33.50 | -04 01 34.5 | 0.9 |
| 12 | 1259 | 18 02 24.84 | -23 01 06.2 | 0.5 | 119 | 3938 | 18 42 33.13 | -04 01 16.0 | 1.0 |
| 13 | 1289 | 18 04 17.39 | -22 53 33.5 | 0.7 | 120 | 3946 | 18 42 53.73 | -04 02 33.6 | 0.9 |
| 14 | 1341 | 18 03 16.99 | -21 45 39.3 | 0.8 | 121 | 3959 | 18 44 43.65 | -04 13 32.8 | 0.8 |
| 15 | 1346 | 18 02 13.75 | -21 32 38.4 | 0.8 | 122 | 3985 | 18 43 51.51 | -04 00 15.3 | 0.9 |
| 16 | 1352 | 18 04 37.05 | -21 47 52.5 | 1.0 | 123 | 3994 | 18 42 56.83 | -03 51 21.2 | 1.0 |
| 17 | 1360 | 18 05 29.32 | -21 48 05.0 | 0.8 | 124 | 4003 | 18 43 35.95 | -03 52 03.3 | 1.0 |
| 18 | 1361 | 18 05 07.71 | -21 44 01.7 | 0.9 | 125 | 4020 | 18 42 15.86 | -03 34 45.5 | 0.4 |
| 19 | 1362 | 18 05 36.97 | -21 46 52.7 | 0.8 | 126 | 4082 | 18 46 18.99 | -03 48 15.7 | 0.8 |
| 20 | 1363 | 18 05 22.6 | -21 44 43.9 | 0.9 | 127 | 4106 | 18 44 22.86 | -03 22 59.5 | 1.1 |
| 21 | 1380 | 18 06 37.21 | -21 37 06.6 | 0.8 | 128 | 4133 | 18 45 13.80 | -03 18 43.9 | 0.8 |
| 22 | 1395 | 18 05 25.71 | -21 19 24.6 | 0.8 | 129 | 4139 | 18 45 25.69 | -03 17 25.4 | 0.8 |
| 23 | 1405 | 18 04 53.31 | -21 06 38.1 | 0.8 | 130 | 4219 | 18 46 37.29 | -02 55 23.8 | 0.8 |
| 24 | 1407 | 18 06 53.76 | -21 17 24.6 | 0.6 | 131 | 4284 | 18 45 59.25 | -02 35 00.7 | 0.9 |
| 25 | 1409 | 18 05 56.88 | -21 03 15.6 | 1.0 | 132 | 4321 | 18 47 09.08 | -02 30 12.3 | 0.9 |
| 26 | 1412 | 18 06 52.57 | -21 04 36.8 | 0.5 | 133 | 4366 | 18 45 20.04 | -02 07 19.3 | 0.8 |
| 27 | 1425 | 18 07 34.20 | -20 26 12.9 | 0.8 | 134 | 4398 | 18 47 40.85 | -02 20 31.2 | 0.9 |
| 28 | 1466 | 18 09 24.77 | -20 15 37.6 | 0.5 | 135 | 4472 | 18 46 33.95 | -01 59 31.8 | 0.8 |
| 29 | 1467 | 18 09 00.30 | -20 11 37.5 | 0.7 | 136 | 4492 | 18 47 47.84 | -02 04 48.9 | 0.9 |
| 30 | 1472 | 18 08 01.76 | -20 01 31.4 | 1.1 | 137 | 4497 | 18 48 29.10 | -02 09 57.8 | 0.5 |
| 31 | 1479 | 18 09 23.13 | -20 08 08.7 | 0.8 | 138 | 4556 | 18 46 53.32 | -01 47 59.2 | 0.7 |
| 32 | 1497 | 18 08 38.51 | -19 51 54.5 | 1.1 | 139 | 4581 | 18 48 06.12 | -01 53 32.3 | 1.0 |
| 33 | 1508 | 18 10 29.00 | -19 55 44.0 | 0.8 | 140 | 4621 | 18 47 15.06 | -01 41 36.1 | 0.9 |
| 34 | 1516 | 18 09 53.11 | -19 47 55.7 | 1.0 | 141 | 4627 | 18 47 32.19 | -01 42 59.2 | 1.0 |
| 35 | 1543 | 18 09 50.65 | -19 37 03.3 | 1.0 | 142 | 4642 | 18 47 04.30 | -01 36 51.1 | 0.9 |
| 36 | 1559 | 18 09 39.95 | -19 26 28.8 | 1.1 | 143 | 4649 | 18 45 09.42 | -01 21 02.7 | 0.8 |
| 37 | 1580 | 18 10 18.59 | -19 24 22.7 | 0.5 | 144 | 4673 | 18 46 25.22 | -01 26 26.8 | 0.5 |
| 38 | 1587 | 18 09 45.84 | -19 17 30.8 | 1.1 | 145 | 4678 | 18 47 09.51 | -01 30 22.3 | 0.5 |
| 39 | 1591 | 18 09 52.01 | -19 17 21.5 | 0.5 | 146 | 4701 | 18 48 45.64 | -01 37 25.9 | 1.1 |
| 40 | 1592 | 18 10 32.84 | -19 22 15.5 | 0.8 | 147 | 4759 | 18 47 53.66 | -01 16 28.6 | 1.0 |
| 41 | 1657 | 18 12 18.83 | -18 39 53.4 | 0.7 | 148 | 4812 | 18 48 42.02 | -01 09 59.9 | 0.9 |
| 42 | 1668 | 18 12 40.36 | -18 37 04.4 | 0.8 | 149 | 4892 | 18 48 20.04 | 00 45 44.3 | 0.8 |
| 43 | 1682 | 18 12 23.81 | -18 22 45.0 | 0.7 | 150 | 5008 | 18 51 44.64 | 00 24 21.7 | 1.0 |
| 44 | 1699 | 18 10 43.55 | -17 58 18.5 | 0.9 | 151 | 5032 | 18 51 14.16 | 00 13 42.8 | 0.8 |
| 45 | 1720 | 18 13 41.39 | -18 12 34.7 | 0.8 | 152 | 5061 | 18 51 32.43 | 00 07 41.7 | 0.5 |
| 46 | 1734 | 18 14 28.49 | -18 12 06.8 | 0.6 | 153 | 5100 | 18 51 24.97 | 00 04 11.1 | 0.5 |

Table 2—Continued

| Number | BGPS ID | R.A. (J2000) | Decl. (J2000) | σ_{rms} (Jy) | Number | BGPS ID | R.A. (J2000) | Decl. (J2000) | σ_{rms} (Jy) |
|--------|---------|--------------|---------------|---------------------|--------|---------|--------------|---------------|---------------------|
| 47 | 1742 | 18 13 11.47 | -17 59 48.6 | 0.8 | 154 | 5167 | 18 52 14.76 | 00 24 46.3 | 0.5 |
| 48 | 1756 | 18 13 03.68 | -17 53 11.4 | 0.4 | 155 | 5170 | 18 50 58.77 | 00 35 19.5 | 0.9 |
| 49 | 1778 | 18 14 39.87 | -17 59 06.4 | 0.6 | 156 | 5230 | 18 52 04.30 | 00 45 02.4 | 0.9 |
| 50 | 1803 | 18 11 51.33 | -17 31 26.4 | 0.8 | 157 | 5240 | 18 51 49.85 | 00 49 02.7 | 0.8 |
| 51 | 1809 | 18 13 48.16 | -17 45 34.4 | 0.8 | 158 | 5252 | 18 52 58.32 | 00 42 42.8 | 0.9 |
| 52 | 1841 | 18 15 07.81 | -17 46 52.7 | 0.9 | 159 | 5265 | 18 53 49.15 | 00 41 28.0 | 0.7 |
| 53 | 1853 | 18 14 36.96 | -17 38 47.2 | 0.9 | 160 | 5270 | 18 53 03.08 | 00 49 31.1 | 0.5 |
| 54 | 1857 | 18 14 28.34 | -17 36 01.8 | 0.8 | 161 | 5373 | 18 53 18.61 | 01 25 16.6 | 0.7 |
| 55 | 1865 | 18 14 01.29 | -17 28 33.3 | 0.8 | 162 | 5501 | 18 55 00.61 | 01 47 24.6 | 0.8 |
| 56 | 1877 | 18 13 47.59 | -17 22 15.8 | 0.8 | 163 | 5516 | 18 55 21.71 | 01 48 45.2 | 0.7 |
| 57 | 1998 | 18 18 09.86 | -16 57 23.7 | 0.5 | 164 | 5572 | 18 56 54.23 | 01 52 48.9 | 0.5 |
| 58 | 2002 | 18 18 03.65 | -16 54 49.7 | 0.7 | 165 | 5577 | 18 56 30.78 | 01 57 10.0 | 1.0 |
| 59 | 2012 | 18 18 08.35 | -16 51 12.7 | 0.7 | 166 | 5594 | 18 56 34.81 | 02 01 14.1 | 1.0 |
| 60 | 2045 | 18 17 08.68 | -16 26 05.7 | 0.9 | 167 | 5691 | 18 55 55.25 | 02 32 43.8 | 0.6 |
| 61 | 2091 | 18 17 23.36 | -16 12 27.4 | 0.7 | 168 | 5720 | 18 58 41.71 | 02 30 57.5 | 0.9 |
| 62 | 2096 | 18 17 51.12 | -16 13 59.8 | 0.7 | 169 | 5722 | 18 57 45.97 | 02 39 02.8 | 0.8 |
| 63 | 2124 | 18 21 12.49 | -16 30 17.5 | 0.6 | 170 | 5782 | 18 57 59.47 | 03 23 59.0 | 0.9 |
| 64 | 2154 | 18 14 48.38 | -15 28 20.0 | 0.6 | 171 | 5836 | 18 59 42.95 | 03 53 45.3 | 0.5 |
| 65 | 2199 | 18 18 56.46 | -15 44 58.5 | 1.0 | 172 | 5869 | 19 01 02.49 | 04 12 06.8 | 0.5 |
| 66 | 2246 | 18 21 08.91 | -15 03 48.2 | 0.6 | 173 | 5896 | 19 01 16.50 | 04 37 01.8 | 0.9 |
| 67 | 2264 | 18 22 23.37 | -14 59 38.3 | 0.8 | 174 | 5919 | 19 01 08.68 | 05 04 28.5 | 0.7 |
| 68 | 2291 | 18 21 15.08 | -14 32 55.3 | 0.9 | 175 | 5922 | 19 02 33.87 | 04 56 40.0 | 0.6 |
| 69 | 2292 | 18 21 09.21 | -14 31 45.5 | 0.8 | 176 | 5941 | 19 03 47.06 | 05 04 00.9 | 0.9 |
| 70 | 2297 | 18 21 30.62 | -14 30 42.6 | 1.0 | 177 | 5993 | 19 04 21.68 | 05 49 47.5 | 0.9 |
| 71 | 2354 | 18 22 59.5 | -13 19 41.4 | 0.9 | 178 | 6017 | 19 04 04.51 | 06 30 12.3 | 1.2 |
| 72 | 2381 | 18 25 21.94 | -13 13 27.4 | 1.0 | 179 | 6023 | 19 05 51.60 | 06 24 42.4 | 0.8 |
| 73 | 2467 | 18 27 08.01 | -12 41 38.3 | 0.8 | 180 | 6086 | 19 06 11.27 | 08 10 31.7 | 0.6 |
| 74 | 2499 | 18 25 44.96 | -12 22 41.7 | 0.9 | 181 | 6110 | 19 11 39.57 | 08 46 30.4 | 0.6 |
| 75 | 2630 | 18 28 23.57 | -11 47 38.3 | 0.9 | 182 | 6111 | 19 10 22.40 | 08 58 44.8 | 1.1 |
| 76 | 2636 | 18 29 14.68 | -11 50 24.0 | 0.9 | 183 | 6131 | 19 12 53.93 | 09 37 11.3 | 1.0 |
| 77 | 2641 | 18 28 19.10 | -11 40 25.5 | 0.9 | 184 | 6137 | 19 11 25.56 | 10 00 03.4 | 0.5 |
| 78 | 2659 | 18 28 10.39 | -11 28 44.2 | 0.7 | 185 | 6153 | 19 11 24.68 | 10 28 43.3 | 1.1 |
| 79 | 2665 | 18 27 44.80 | -11 14 52.2 | 0.9 | 186 | 6166 | 19 13 40.95 | 10 54 57.8 | 0.8 |
| 80 | 2696 | 18 30 09.87 | -11 12 39.1 | 1.0 | 187 | 6188 | 19 15 12.95 | 11 10 21.5 | 1.0 |
| 81 | 2711 | 18 29 59.62 | -11 00 22.2 | 0.9 | 188 | 6208 | 19 17 13.41 | 11 16 14.0 | 1.1 |
| 82 | 2713 | 18 30 11.16 | -11 01 10.4 | 0.9 | 189 | 6225 | 19 16 58.42 | 11 47 20.2 | 1.0 |
| 83 | 2837 | 18 30 35.29 | -09 34 40.1 | 0.9 | 190 | 6258 | 19 19 48.70 | 14 01 11.2 | 0.8 |
| 84 | 2858 | 18 30 38.33 | -09 12 43.8 | 0.8 | 191 | 6280 | 19 22 48.67 | 13 53 34.3 | 0.9 |
| 85 | 2865 | 18 32 44.16 | -09 24 33.6 | 0.9 | 192 | 6298 | 19 22 41.65 | 14 09 59.4 | 1.0 |
| 86 | 2890 | 18 31 44.72 | -09 08 32.8 | 0.9 | 193 | 6304 | 19 22 33.86 | 14 13 35.1 | 0.9 |
| 87 | 2904 | 18 31 10.67 | -08 54 17.6 | 0.8 | 194 | 6323 | 19 23 06.95 | 14 20 11.1 | 0.5 |
| 88 | 3022 | 18 35 21.67 | -08 50 15.1 | 0.9 | 195 | 6338 | 19 22 46.39 | 14 30 28.0 | 0.7 |
| 89 | 3034 | 18 34 00.19 | -08 35 54.0 | 0.8 | 196 | 6346 | 19 23 30.08 | 14 26 34.6 | 0.8 |
| 90 | 3071 | 18 34 39.30 | -08 31 35.3 | 0.9 | 197 | 6376 | 19 23 26.56 | 14 40 14.1 | 0.8 |
| 91 | 3081 | 18 34 35.95 | -08 29 32.2 | 0.9 | 198 | 6380 | 19 21 17.62 | 15 11 50.1 | 1.0 |
| 92 | 3153 | 18 35 12.45 | -08 17 35.5 | 0.8 | 199 | 6387 | 19 23 12.41 | 15 13 30.5 | 1.1 |

Table 2—Continued

| Number | BGPS ID | R.A. (J2000) | Decl. (J2000) | σ_{rms} (Jy) | Number | BGPS ID | R.A. (J2000) | Decl. (J2000) | σ_{rms} (Jy) |
|--------|---------|--------------|---------------|---------------------|--------|---------|--------------|---------------|---------------------|
| 93 | 3202 | 18 35 22.49 | -08 01 18.7 | 0.9 | 200 | 6414 | 19 29 18.22 | 17 56 19.0 | 0.9 |
| 94 | 3208 | 18 35 23.45 | -07 59 32.6 | 0.7 | 201 | 6416 | 19 30 30.35 | 17 48 26.1 | 0.8 |
| 95 | 3209 | 18 34 08.83 | -07 49 33.7 | 0.9 | 202 | 6424 | 19 30 05.13 | 17 57 28.0 | 1.0 |
| 96 | 3274 | 18 35 35.52 | -07 41 46.1 | 0.9 | 203 | 6429 | 19 30 10.65 | 18 11 06.7 | 1.0 |
| 97 | 3284 | 18 35 08.61 | -07 35 04.3 | 0.9 | 204 | 6433 | 19 30 22.74 | 18 20 20.9 | 0.6 |
| 98 | 3383 | 18 35 39.86 | -07 18 32.7 | 0.6 | 205 | 6437 | 19 30 29.80 | 18 20 39.7 | 0.9 |
| 99 | 3394 | 18 36 50.31 | -07 24 44.5 | 0.6 | 206 | 6445 | 19 31 28.15 | 18 34 08.9 | 1.0 |
| 100 | 3402 | 18 35 50.97 | -07 13 29.1 | 0.8 | 207 | 6451 | 19 31 49.34 | 18 43 01.6 | 1.1 |
| 101 | 3413 | 18 36 12.90 | -07 12 06.6 | 0.8 | 208 | 6455 | 19 32 12.69 | 18 59 01.5 | 1.1 |
| 102 | 3437 | 18 36 26.92 | -07 05 07.7 | 0.5 | 209 | 6470 | 19 38 16.80 | 21 08 02.2 | 0.6 |
| 103 | 3466 | 18 36 28.09 | -06 47 51.0 | 0.8 | 210 | 6474 | 19 38 58.22 | 22 46 34.6 | 0.9 |
| 104 | 3503 | 18 38 08.47 | -06 46 40.8 | 1.0 | 211 | 6476 | 19 43 42.32 | 23 20 20.3 | 0.9 |
| 105 | 3504 | 18 38 55.53 | -06 52 18.1 | 0.7 | 212 | 6479 | 19 43 50.15 | 23 28 59.7 | 0.9 |
| 106 | 3505 | 18 37 30.70 | -06 41 17.8 | 0.8 | 213 | 6492 | 19 43 30.46 | 23 57 44.9 | 1.0 |
| 107 | 3528 | 18 37 20.83 | -06 31 55.6 | 0.8 | 214 | 6501 | 19 50 03.19 | 26 38 23.3 | 0.8 |

Table 3. Observed properties of 95 GHz class I methanol maser sources detected – The full table is available in the online journal.

| Number | Gaussian Fit | | | | S_{int}^m (Jy km s ⁻¹) |
|--------|------------------------------------|-------------------------------------|---------------------------------|-----------|---|
| | V_{LSR} (km s ⁻¹) | ΔV (km s ⁻¹) | S (Jy km s ⁻¹) | P (Jy) | |
| (1) | (2) | (3) | (4) | (5) | (6) |
| 11 | 20.36(0.08) | 0.89(0.21) | 5.8(1.1) | 6.1 | 23.4 |
| ... | 21.35(0.07) | 0.51(0.16) | 3.2(1.0) | 5.8 | |
| ... | 22.63(0.06) | 0.97(0.15) | 10.4(1.5) | 10.0 | |
| ... | 24.02(0.18) | 1.08(0.43) | 4.1(1.4) | 3.5 | |
| 13 | 20.08(0.89) | 11.54(2.26) | 15.0(2.5) | 1.2 | 17.3 |
| ... | 20.62(0.12) | 0.87(0.30) | 2.3(0.8) | 2.5 | |
| 20 | 98.48(0.30) | 2.71(0.70) | 6.9(1.5) | 2.4 | 6.9 |
| 22 | -0.46(0.05) | 0.26(0.22) | 1.5(0.6) | 5.4 | 20.9 |
| ... | 0.39(0.03) | 0.73(0.10) | 8.2(1.1) | 10.7 | |
| ... | 1.58(0.12) | 0.78(0.36) | 2.5(1.3) | 3.0 | |
| ... | 1.80(0.84) | 5.71(1.88) | 8.7(2.8) | 1.4 | |
| 29 | 11.95(0.20) | 2.93(0.47) | 8.4(1.2) | 2.7 | 8.4 |
| 31 | 32.70(0.01) | 0.33(0.01) | 15.2(1.0) | 43.4 | 45.3 |
| ... | 32.57(0.06) | 1.44(0.17) | 13.9(1.3) | 9.1 | |
| ... | 34.93(0.04) | 1.23(0.09) | 16.1(1.0) | 12.3 | |
| 32 | 66.91(0.19) | 9.38(0.46) | 78.3(3.4) | 7.8 | 78.3 |
| 33 | -3.42(0.21) | 8.90(0.40) | 80.9(3.7) | 8.5 | 113.4 |
| ... | -6.31(0.05) | 0.96(0.11) | 15.0(3.4) | 14.7 | |
| ... | -7.59(0.18) | 1.75(0.36) | 17.5(4.2) | 9.4 | |
| 39 | 21.81(0.05) | 1.16(0.12) | 6.5(0.6) | 5.2 | 6.5 |
| 41 | 43.00(0.13) | 2.59(0.31) | 10.3(1.1) | 3.7 | 10.3 |
| 43 | 49.47(0.18) | 1.64(0.43) | 4.2(1.0) | 2.4 | 8.7 |
| ... | 53.14(0.44) | 3.10(1.14) | 4.4(1.3) | 1.3 | |
| 47 | 19.83(0.05) | 0.88(0.12) | 8.2(0.9) | 8.8 | 24.2 |
| ... | 21.17(0.13) | 0.90(0.39) | 3.6(2.2) | 3.8 | |
| ... | 22.76(0.22) | 2.20(0.49) | 12.4(2.5) | 5.3 | |
| 49 | 12.64(0.13) | 2.26(0.32) | 7.9(0.9) | 3.3 | 9.8 |
| ... | 15.02(0.08) | 0.63(0.18) | 1.9(0.5) | 2.9 | |
| 50 | 31.66(0.03) | 0.47(0.08) | 4.4(0.9) | 8.7 | 27.6 |
| ... | 32.71(0.12) | 0.57(0.36) | 1.4(1.1) | 2.3 | |
| ... | 32.94(0.19) | 3.87(0.40) | 21.8(2.3) | 5.3 | |
| 51 | 55.27(0.14) | 1.20(0.30) | 5.3(1.6) | 4.2 | 27.1 |
| ... | 57.35(0.08) | 2.13(0.21) | 21.7(1.8) | 9.6 | |
| 53 | 43.95(0.01) | 0.42(0.03) | 8.7(0.6) | 19.4 | 8.7 |
| 54 | 36.18(0.21) | 2.11(0.49) | 6.0(1.2) | 2.7 | 6.0 |
| 55 | 49.59(0.03) | 0.85(0.11) | 9.7(1.9) | 10.8 | 57.5 |
| ... | 49.62(0.05) | 3.32(0.18) | 47.8(2.2) | 13.5 | |
| 57 | 81.38(0.05) | 0.40(0.13) | 1.3(0.4) | 3.0 | 4.3 |
| ... | 82.78(0.12) | 1.22(0.31) | 3.0(0.6) | 2.3 | |
| 63 | 20.66(0.14) | 1.74(0.43) | 4.8(1.5) | 2.6 | 11.8 |
| ... | 24.87(1.38) | 7.76(2.91) | 7.0(2.5) | 0.9 | |
| 69 | 61.37(0.03) | 0.84(0.07) | 17.1(1.3) | 19.0 | 29.9 |
| ... | 60.36(0.07) | 0.72(0.17) | 6.4(1.6) | 8.3 | |

Table 3—Continued

| Number | Gaussian Fit | | | | S_{int}^m (Jy km s ⁻¹) |
|--------|------------------------------------|-------------------------------------|---------------------------------|-----------|---|
| | V_{LSR} (km s ⁻¹) | ΔV (km s ⁻¹) | S (Jy km s ⁻¹) | P (Jy) | |
| (1) | (2) | (3) | (4) | (5) | (6) |
| ... | 58.68(0.20) | 1.84(0.54) | 6.4(1.5) | 3.3 | |
| 72 | 46.08(0.02) | 0.30(0.06) | 6.2(1.5) | 19.4 | 21.7 |
| ... | 46.74(0.06) | 0.98(0.13) | 15.5(1.9) | 14.9 | |
| 73 | 64.79(0.08) | 1.18(0.26) | 10.4(4.6) | 8.3 | 43.6 |
| ... | 66.17(0.02) | 0.51(0.07) | 7.9(1.5) | 14.4 | |
| ... | 65.99(0.29) | 3.03(0.34) | 25.2(6.0) | 7.8 | |
| 74 | 58.78(0.54) | 4.82(1.09) | 11.6(2.8) | 2.3 | 27.3 |
| ... | 59.73(0.04) | 1.19(0.12) | 15.7(2.0) | 12.3 | |
| 76 | 41.38(0.06) | 0.67(0.14) | 4.4(0.8) | 6.1 | 72.3 |
| ... | 43.51(0.03) | 0.87(0.08) | 18.6(3.0) | 20.2 | |
| ... | 44.06(0.07) | 2.28(0.10) | 49.2(3.4) | 20.3 | |
| 77 | 63.14(0.04) | 0.66(0.10) | 6.8(1.0) | 9.7 | 25.5 |
| ... | 64.40(0.05) | 1.04(0.15) | 14.0(1.7) | 12.7 | |
| ... | 65.92(0.18) | 1.20(0.44) | 4.8(1.5) | 3.8 | |
| 78 | 42.82(0.24) | 7.94(0.58) | 13.0(0.8) | 1.5 | 13.0 |
| 83 | 50.67(0.04) | 0.85(0.12) | 10.6(1.5) | 11.7 | 54.8 |
| ... | 51.72(0.02) | 0.66(0.05) | 14.7(1.3) | 21.0 | |
| ... | 52.19(0.23) | 5.11(0.47) | 29.5(2.8) | 5.4 | |
| 90 | 96.91(0.02) | 1.24(0.07) | 24.0(1.5) | 18.2 | 136.3 |
| ... | 99.94(0.02) | 0.42(0.04) | 7.4(0.7) | 16.6 | |
| ... | 101.38(0.13) | 5.81(0.31) | 73.7(3.0) | 11.9 | |
| ... | 101.50(0.03) | 0.40(0.08) | 3.4(0.8) | 8.0 | |
| ... | 102.63(0.02) | 1.05(0.05) | 27.7(1.6) | 24.8 | |
| 93 | 72.98(0.47) | 6.30(1.18) | 14.7(2.3) | 2.2 | 17.6 |
| ... | 73.14(0.04) | 0.42(0.10) | 3.0(0.7) | 6.6 | |
| 94 | 69.72(0.11) | 2.76(0.26) | 12.9(1.1) | 4.4 | 12.9 |
| 97 | 113.52(0.02) | 0.63(0.05) | 16.1(1.6) | 24.1 | 80.7 |
| ... | 114.33(0.05) | 2.34(0.09) | 58.9(2.4) | 23.7 | |
| ... | 116.58(0.05) | 0.70(0.12) | 5.6(1.0) | 7.6 | |
| 98 | 51.13(0.06) | 0.52(0.14) | 2.3(0.7) | 4.1 | 11.8 |
| ... | 52.19(0.14) | 0.98(0.40) | 2.5(1.0) | 2.4 | |
| ... | 52.08(0.87) | 7.15(2.44) | 7.1(1.9) | 0.9 | |
| 99 | 113.26(0.19) | 2.09(0.44) | 4.8(0.9) | 2.2 | 4.8 |
| 101 | 108.19(0.05) | 0.84(0.11) | 9.2(1.2) | 10.4 | 68.4 |
| ... | 109.45(0.13) | 1.02(0.14) | 5.7(1.7) | 5.3 | |
| ... | 111.20(0.08) | 1.83(0.17) | 23.5(2.5) | 12.1 | |
| ... | 112.66(0.11) | 0.77(0.21) | 6.7(2.0) | 8.1 | |
| ... | 113.35(0.07) | 0.52(0.18) | 5.5(1.8) | 9.8 | |
| ... | 114.13(0.05) | 0.73(0.17) | 8.7(1.8) | 11.2 | |
| ... | 114.94(0.06) | 0.32(0.15) | 1.4(1.0) | 4.1 | |
| ... | 115.69(0.55) | 2.30(0.21) | 8.0(1.8) | 3.3 | |
| 102 | 46.69(0.24) | 2.59(0.58) | 4.2(0.8) | 1.5 | 4.2 |
| 104 | 93.88(0.06) | 0.61(0.15) | 6.8(1.4) | 10.6 | 23.2 |

Table 3—Continued

| Number | Gaussian Fit | | | | S_{int}^m (Jy km s ⁻¹) |
|--------|------------------------------------|-------------------------------------|---------------------------------|-----------|---|
| | V_{LSR} (km s ⁻¹) | ΔV (km s ⁻¹) | S (Jy km s ⁻¹) | P (Jy) | |
| (1) | (2) | (3) | (4) | (5) | (6) |
| ... | 94.38(0.07) | 0.22(0.11) | 1.7(1.2) | 7.4 | |
| ... | 96.19(0.11) | 2.03(0.27) | 14.6(1.6) | 6.7 | |
| 114 | 104.52(0.33) | 4.89(0.77) | 13.0(2.3) | 2.3 | 14.3 |
| ... | 104.52(0.09) | 0.38(0.09) | 1.3(0.5) | 3.2 | |
| 116 | 45.28(0.05) | 0.53(0.11) | 4.2(0.7) | 7.5 | 4.2 |
| 117 | 99.29(0.44) | 3.70(1.03) | 6.8(1.6) | 1.7 | 6.8 |
| 120 | 79.07(0.09) | 0.43(0.21) | 1.7(0.8) | 3.7 | 16.5 |
| ... | 79.71(0.07) | 0.48(0.17) | 2.6(0.9) | 5.0 | |
| ... | 80.02(0.50) | 5.85(1.26) | 12.2(2.2) | 2.0 | |
| 125 | 90.69(0.06) | 0.39(0.16) | 0.8(0.3) | 1.9 | 5.5 |
| ... | 90.26(0.77) | 6.87(1.90) | 4.7(1.1) | 0.6 | |
| 126 | 76.43(0.08) | 1.56(0.18) | 10.1(1.0) | 6.1 | 10.1 |
| 128 | 60.28(0.01) | 0.51(0.02) | 14.8(0.6) | 27.3 | 14.8 |
| 133 | 93.10(0.09) | 1.05(0.20) | 4.8(0.8) | 4.3 | 4.8 |
| 134 | 101.16(0.09) | 0.61(0.21) | 2.6(0.8) | 3.9 | 45.1 |
| ... | 105.13(0.09) | 3.65(0.23) | 39.9(2.0) | 10.3 | |
| ... | 109.35(0.43) | 1.75(1.02) | 2.7(1.4) | 1.4 | |
| 135 | 103.69(0.07) | 0.53(0.17) | 2.0(0.6) | 3.6 | 10.2 |
| ... | 105.54(0.08) | 1.43(0.19) | 8.2(0.9) | 5.4 | |
| 143 | 50.32(0.07) | 0.67(0.17) | 2.9(0.6) | 4.1 | 2.9 |
| 144 | 31.35(0.27) | 2.67(0.68) | 4.0(0.9) | 1.4 | 5.6 |
| ... | 35.75(0.68) | 2.72(1.71) | 1.6(0.9) | 0.6 | |
| 148 | 96.30(0.08) | 3.62(0.20) | 36.4(1.7) | 9.4 | 36.4 |
| 153 | 83.22(0.07) | 1.55(0.17) | 6.3(0.6) | 3.8 | 6.3 |
| 154 | 104.09(0.49) | 7.29(1.17) | 9.5(1.3) | 1.2 | 9.5 |
| 158 | 106.46(0.25) | 3.63(0.70) | 12.6(1.9) | 3.2 | 14.9 |
| ... | 106.47(0.11) | 0.58(0.31) | 1.8(1.1) | 2.9 | |
| 160 | 60.26(0.01) | 0.31(0.05) | 2.6(0.3) | 7.9 | 6.0 |
| ... | 61.77(0.04) | 0.76(0.11) | 3.4(0.4) | 4.2 | |
| 161 | 58.09(0.09) | 5.01(0.18) | 61.4(2.3) | 11.5 | 64.9 |
| ... | 60.25(0.10) | 0.99(0.29) | 3.6(1.3) | 3.4 | |
| 164 | 52.43(0.23) | 4.82(0.54) | 11.4(1.1) | 2.2 | 11.4 |
| 172 | 63.09(0.39) | 2.49(0.91) | 4.2(1.4) | 1.6 | 8.1 |
| ... | 65.96(0.32) | 2.05(0.70) | 3.8(1.3) | 1.7 | |
| 181 | 58.10(0.19) | 3.49(0.49) | 10.0(1.2) | 2.7 | 11.1 |
| ... | 58.19(0.05) | 0.27(0.16) | 1.0(0.4) | 3.6 | |
| 194 | 67.39(0.26) | 2.88(0.61) | 4.8(0.9) | 1.6 | 4.8 |
| 200 | 19.51(0.25) | 0.18(0.05) | 2.2(0.3) | 11.1 | 16.3 |
| ... | 20.35(0.55) | 2.51(0.38) | 5.7(1.3) | 2.1 | |
| ... | 22.19(0.04) | 0.75(0.11) | 8.4(1.6) | 10.5 | |
| 209 | 32.01(0.17) | 1.10(0.41) | 2.1(0.6) | 1.8 | 4.4 |
| ... | 33.49(0.05) | 0.53(0.12) | 2.3(0.5) | 4.1 | |
| 210 | 36.28(0.11) | 1.37(0.27) | 6.7(1.1) | 4.6 | 10.0 |

Table 3—Continued

| Number | Gaussian Fit | | | | S_{int}^m (Jy km s ⁻¹) |
|--------|------------------------------------|-------------------------------------|---------------------------------|-------------|---|
| | V_{LSR} (km s ⁻¹) | ΔV (km s ⁻¹) | S (Jy km s ⁻¹) | P (Jy) | |
| (1) | (2) | (3) | (4) | (5) | (6) |
| ... | 38.21(0.09) | 0.72(0.21) | 3.3(0.8) | 4.2 | |
| 212 | 27.23(0.12) | 1.59(0.26) | 14.4(2.2) | 8.5 | 23.7 |
| ... | 28.88(0.18) | 1.20(0.39) | 5.8(2.2) | 4.6 | |
| ... | 30.70(0.11) | 0.91(0.28) | 3.4(0.9) | 3.5 | |

Note. — Column (1): source number. Columns. (2)-(5): the velocity at peak V_{LSR} , the line FWHM ΔV , the integrated intensity S , and the peak flux density P of each maser feature estimated from Gaussian fits to the 95 GHz class I methanol maser lines. The formal error from the Gaussian fit is given in parenthesis. Col. (6): the total integrated flux density S_{int}^m (Jy) of the maser spectrum obtained from summing the integrated flux density of all maser features in each source in column (4).

Table 4. Sources detected as class I methanol masers in previous surveys.

| Number | Source | Detections | | Referee |
|--------|-----------------|------------|--------|--|
| | | 44 GHz | 95 GHz | |
| 22 | 18024-2119 | Y | N | Fontani et al. (2010) |
| 32 | G10.47+0.03 | Y | – | Kurtz et al. (2004) |
| 33 | G10.62-0.38 | Y | – | Kurtz et al. (2004) |
| 43 | EGO G12.20-0.03 | | Y | Chen et al. (2011) |
| 51 | EGO G12.91-0.03 | | Y | Chen et al. (2011) |
| 69 | EGO G16.59-0.05 | Y | Y | Slysh et al. (1994); Val'tts et al. (2000) |
| 73 | EGO G18.89-0.47 | Y | Y | Chen et al. (2011) |
| 74 | EGO G19.01-0.03 | Y | Y | Chen et al. (2011) |
| 76 | EGO G19.88-0.53 | – | Y | Chen et al. (2011) |
| 83 | EGO G22.04+0.22 | Y | Y | Chen et al. (2011) |
| 90 | G23.43-0.19 | Y | – | Slysh et al. (1994) |
| 93 | EGO G23.96-0.11 | Y | – | Chen et al. (2011) |
| 94 | EGO G24.00-0.10 | – | Y | Chen et al. (2011) |
| 97 | EGO G24.33+0.14 | – | Y | Chen et al. (2011) |
| 98 | EGO G24.63+0.15 | – | Y | Chen et al. (2011) |
| 101 | W42 | Y | – | Bachiller et al. (1990) |
| 104 | EGO G25.38-0.15 | – | Y | Chen et al. (2011) |
| 161 | EGO G34.41+0.24 | – | Y | Chen et al. (2011) |
| 181 | EGO G43.04-0.45 | Y | – | Chen et al. (2011) |
| 194 | EGO G49.27-0.34 | Y | – | Cyganowski et al. (2009) |

Table 5. The related parameters of the detected class I methanol masers.

| Number | Distance (kpc) | Luminosity ($10^{-6} L_{\odot}$) | BGPS source | | | | IRDC | Class II maser |
|--------------------|-------------------|---------------------------------------|-------------|----------------------|--|---|------|----------------|
| | | | ID | M (M_{\odot}) | n(H ₂) (10^3 cm^{-3}) | N(H ₂) (10^{22} cm^{-2}) | | |
| (1) | (2) | (3) | (4) | (5) | (6) | (7) | (8) | (9) |
| 11 | 13.0 | 124.3 | 1251 | 4900 | 1.6 | 1.5 | N | N |
| 13 | 3.4 | 6.3 | 1289 | 310 | 5.3 | 1.4 | Y | N |
| 20 ^D | 4.3 | 4.0 | 1363 | 370 | 4.8 | 1.4 | Y | N |
| 22 ^{G,D} | 5.2 | 17.8 | 1395 | 2100 | 1.5 | 1.1 | Y | Y |
| 29 ^S | 1.9 | 0.9 | 1467 | 560 | 3.0 | 1.1 | Y | N |
| 31 | 12.7 | 229.6 | 1479 | 11000 | 0.8 | 1.2 | N | Y |
| 32 | 11.2 | 308.6 | 1497 | 52000 | 24.6 | 20.8 | N | Y |
| 33 | 4.0* | 57.0 | 1508 | 6300 | 113.9 | 28.7 | Y | Y |
| 39 | 13.7 | 38.2 | 1591 | 2000 | – | – | N | N |
| 41 ^G | 12.2 | 48.0 | 1657 | 5000 | 1.6 | 1.6 | N | Y |
| 43 ^G | 12.0 | 39.2 | 1682 | 5900 | 0.8 | 1.0 | N | Y |
| 47 ^G | 2.7 | 5.6 | 1742 | 820 | 3.0 | 1.3 | N | Y |
| 49 | 14.7 | 66.6 | 1778 | 14000 | 0.4 | 0.8 | N | N |
| 50 ^G | 2.3 | 4.6 | 1803 | 830 | 15.9 | 3.9 | Y | Y |
| 51 ^S | 4.6 | 17.9 | 1809 | 1500 | 2.0 | 1.2 | Y | Y |
| 53 | 12.4 | 42.0 | 1853 | 5700 | 0.5 | 0.8 | N | N |
| 54 ^S | 3.5 | 2.3 | 1857 | 540 | 1.6 | 0.7 | Y | N |
| 55 ^{G,S} | 4.1 | 30.4 | 1865 | 1700 | 4.4 | 2.1 | Y | Y |
| 57 | 11.0 | 16.4 | 1998 | 3000 | 20.7 | 7.2 | N | N |
| 63 | 13.7 | 69.5 | 2124 | 11000 | 0.8 | 1.3 | N | N |
| 69 ^{G,S} | 4.3 | 17.4 | 2292 | 1300 | 17.6 | 4.8 | Y | Y |
| 72 | 12.5 | 106.4 | 2381 | 11000 | 0.5 | 0.9 | N | N |
| 73 ^{G,S} | 3.8 | 19.8 | 2467 | 2800 | 1.8 | 1.4 | Y | Y |
| 74 ^G | 12.0 | 123.6 | 2499 | 6800 | 1.6 | 1.7 | N | Y |
| 76 ^{G,D} | 3.3 | 24.7 | 2636 | 1100 | 16.5 | 4.4 | Y | Y |
| 77 ^{D,S} | 4.1 | 13.5 | 2641 | 1100 | 3.5 | 1.6 | Y | N |
| 78 ^D | 12.6 | 64.9 | 2659 | 19000 | 1.6 | 2.4 | N | – |
| 83 ^G | 3.3 | 18.8 | 2837 | 1000 | 1.5 | 0.9 | Y | Y |
| 90 ^G | 5.9 | 149.1 | 3071 | 9600 | 1.0 | 1.4 | Y | Y |
| 93 ^G | 11.4 | 72.0 | 3202 | 8600 | 1.1 | 1.4 | N | Y |
| 94 ^G | 11.4 | 52.7 | 3208 | 4800 | 2.6 | 2.1 | N | Y |
| 97 ^{G,S} | 9.5 | 228.9 | 3284 | 7800 | 4.3 | 3.5 | Y | Y |
| 98 ^S | 3.3 | 4.1 | 3383 | 430 | 3.4 | 1.1 | Y | N |
| 99 | 5.8 | 5.1 | 3394 | 4800 | 2.8 | 2.2 | Y | – |
| 101 | 9.6 | 199.1 | 3413 | 32000 | 3.3 | 4.7 | N | – |
| 102 | 12.2 | 19.6 | 3437 | 11000 | 1.5 | 1.9 | N | – |
| 104 | 5.1 | 18.9 | 3503 | 1600 | 11.6 | 4.0 | Y | – |
| 114 | 5.5 | 13.0 | 3833 | 740 | 2.4 | 1.1 | Y | – |
| 116 ^S | 2.9 | 1.1 | 3876 | 91 | 10.5 | 1.4 | Y | – |
| 117 ^{G,S} | 5.3 | 6.0 | 3897 | 2000 | 0.6 | 0.6 | Y | Y |
| 120 | 4.5 | 10.5 | 3946 | 790 | 2.7 | 1.2 | Y | – |
| 125 | 4.9 | 4.2 | 4020 | 280 | 4.7 | 1.2 | Y | – |
| 126 | 10.4 | 34.5 | 4082 | 820 | 1.9 | 0.9 | N | – |

Table 5—Continued

| Number | Distance | Luminosity | BGPS source | | | | IRDC | Class II maser |
|------------------|----------|------------------------------------|-------------|-------------------|-------------------------------------|--------------------------------------|------|----------------|
| | | | ID | M | n(H ₂) | N(H ₂) | | |
| (1) | (kpc) | (10 ⁻⁶ L _⊙) | (4) | (M _⊙) | (10 ³ cm ⁻³) | (10 ²² cm ⁻²) | (8) | (9) |
| 128 | 3.6 | 6.0 | 4133 | 370 | 0.8 | 0.4 | Y | – |
| 133 | 5.1 | 4.0 | 4366 | 1000 | 0.6 | 0.5 | Y | – |
| 134 ^S | 5.7 | 46.1 | 4398 | 5000 | 1.4 | 1.4 | Y | – |
| 135 | 8.7 | 24.4 | 4472 | 19000 | 0.5 | 1.1 | N | – |
| 143 | 3.1 | 0.9 | 4649 | 35 | – | – | Y | – |
| 144 | 12.3 | 26.6 | 4673 | 6400 | 0.4 | 0.7 | N | – |
| 148 ^D | 5.3 | 32.1 | 4812 | 2200 | 1.3 | 1.0 | Y | – |
| 153 ^D | 9.4 | 17.4 | 5100 | 5900 | 0.6 | 0.8 | N | – |
| 154 ^D | 5.7 | 9.7 | 5167 | 4400 | 0.9 | 1.0 | Y | – |
| 158 ^S | 6.5 | 19.1 | 5252 | 4300 | 0.7 | 0.9 | Y | – |
| 160 | 10.3 | 19.9 | 5270 | 2300 | 0.3 | 0.4 | N | – |
| 161 | 10.4 | 220.7 | 5373 | 44000 | 1.6 | 3.2 | N | – |
| 164 | 10.6 | 40.2 | 5572 | 1700 | 4.3 | 2.1 | N | – |
| 172 ^S | 9.5 | 22.8 | 5869 | 8200 | 2.7 | 2.6 | N | – |
| 181 | 8.6 | 25.8 | 6110 | 2500 | 6.6 | 3.2 | N | – |
| 194 ^S | 5.5* | 4.6 | 6323 | 3600 | 7.7 | 3.2 | N | – |
| 200 ^D | 1.6 | 1.3 | 6414 | 280 | 5.6 | 2.3 | Y | – |
| 209 | 3.0 | 1.2 | 6470 | 110 | 8.6 | 1.3 | Y | – |
| 210 ^S | 4.4* | 6.1 | 6474 | 350 | 12.8 | 2.5 | N | – |
| 212 | 5.9 | 25.9 | 6479 | 3200 | 8.8 | 4.1 | N | – |

Note. — Column (1): source number. The sources which are marked by *G*, *D* or *S* overlaid with that in Green & McClure-Griffiths (2011), Dunham et al. (2011b) or Schlingman et al. (2011), respectively. Column (2): the kinematic distance for the source, estimated from the Galactic rotation curve of Reid et al. (2009). For sources overlapped with Green & McClure-Griffiths (2011), we adopted the distances estimated from their work. For the sources (marked by *) of which distances cannot be derived from the Galactic rotation curve, a distance of 4 kpc is adopted for source with an IRDC association (N33), and that determined in Schlingman et al. (2011) for the other two sources (N194 and N210). Column (3): the integrated luminosity of 95 GHz methanol maser. Columns (4) – (7): the ID number of BGPS source in the BGPS catalog, the derived gas mass and averaged H₂ volume and column densities of the BGPS source, respectively. The gas volume and column densities can not be determined due to absence of radius information for the sources which are unresolved by the BGPS beam, we marked them with “–”. Column (8): association with IRDC: Y = Yes, N = No. Column (9): association with a 6.7 GHz methanol maser for which a precise position has been measured. The positions of the 6.7 GHz class II methanol masers were identified from published 6.7 GHz maser catalogs (Caswell 2009; Caswell et al. 2010; Green et al. 2010; Caswell et al. 2011 ; Green et al. 2012): Y = Yes, N = No, “–” = no information.

Table 6. Trends with star formation activity for sources with and without methanol masers

| Property | Group | mean | standard deviation | minimum | median | maximum |
|--|--------------|------|--------------------|---------|--------|---------|
| With and without class I methanol masers | | | | | | |
| $\log(N_{H_2}^{beam})$ [cm^{-2}] | class I | 22.7 | 0.4 | 21.9 | 22.7 | 23.8 |
| | no class I | 21.9 | 0.3 | 21.4 | 21.9 | 22.7 |
| $\log(S_{int})$ [Jy] | class I | 0.7 | 0.4 | -0.6 | 0.7 | 1.5 |
| | no class I | 0.0 | 0.4 | -0.9 | 0.0 | 1.1 |
| Radius (") | class I | 57.8 | 25. 1 | 15.7 | 56.0 | 128.7 |
| | no class I | 49.3 | 21.4 | 5.1 | 46.3 | 113.3 |
| Class I methanol masers with and without class II maser associations | | | | | | |
| $\log(N_{H_2}^{beam})$ [cm^{-2}] | only class I | 22.5 | 0.2 | 22.2 | 22.6 | 22.8 |
| | class I+II | 22.9 | 0.3 | 22.5 | 22.8 | 23.8 |
| $\log(S_{int})$ [Jy] | only class I | 0.48 | 0.29 | -0.09 | 0.47 | 1.07 |
| | class I+II | 0.86 | 0.31 | 0.41 | 0.79 | 1.49 |

Table 7. The distributions of class I methanol maser numbers with BGPS source parameters

| Range | In our observing sample | | | In the full BGPS catalog | |
|----------------------------------|-------------------------|---------------|----------------|--------------------------|---------------------|
| | detections | total numbers | detection rate | total numbers | expected detections |
| $\log(N_{H_2}^{beam}) [cm^{-2}]$ | | | | | |
| 21.0–21.2 | – | – | – | 1 | 0 |
| 21.2–21.4 | – | – | – | 88 | 0 |
| 21.4–21.6 | 0 | 1 | 0.00 | 717 | 0 |
| 21.6–21.8 | 0 | 11 | 0.00 | 2021 | 0 |
| 21.8–22.0 | 1 | 46 | 0.02 | 2303 | 50 |
| 22.0–22.2 | 6 | 45 | 0.13 | 1451 | 193 |
| 22.2–22.4 | 6 | 36 | 0.17 | 804 | 134 |
| 22.4–22.6 | 11 | 29 | 0.38 | 458 | 174 |
| 22.6–22.8 | 17 | 23 | 0.74 | 240 | 177 |
| 22.8–23.0 | 13 | 14 | 0.93 | 142 | 132 |
| 23.0–23.2 | 5 | 5 | 1.00 | 69 | 69 |
| 23.2–23.4 | 1 | 1 | 1.00 | 34 | 34 |
| 23.4–23.6 | 1 | 1 | 1.00 | 8 | 8 |
| 23.6–23.8 | 2 | 2 | 1.00 | 11 | 11 |
| 23.8–24.0 | – | – | – | 7 | 7 |
| 24.0–24.2 | – | – | – | 4 | 4 |
| 24.4–24.6 | – | – | – | 1 | 1 |
| sum | | | | | 995 |
| $\log(S_{int}) [Jy]$ | | | | | |
| -1.4–-1.2 | – | – | – | 10 | 0 |
| -1.2–-1.0 | – | – | – | 109 | 0 |
| -1.0–-0.8 | 0 | 2 | 0.00 | 410 | 0 |
| -0.8–-0.6 | 0 | 2 | 0.00 | 771 | 0 |
| -0.6–-0.4 | 1 | 25 | 0.04 | 1128 | 45 |
| -0.4–-0.2 | 1 | 19 | 0.05 | 1450 | 76 |
| -0.2–0.0 | 4 | 28 | 0.14 | 1296 | 185 |
| 0.0–0.2 | 3 | 26 | 0.12 | 1103 | 127 |
| 0.2–0.4 | 6 | 30 | 0.20 | 784 | 157 |
| 0.4–0.6 | 11 | 31 | 0.35 | 531 | 188 |
| 0.6–0.8 | 14 | 23 | 0.61 | 330 | 201 |
| 0.8–1.0 | 11 | 13 | 0.85 | 223 | 189 |
| 1.0–1.2 | 6 | 9 | 0.67 | 115 | 77 |
| 1.2–1.4 | 2 | 2 | 1.00 | 47 | 47 |
| 1.4–1.6 | 4 | 4 | 1.00 | 27 | 27 |
| 1.6–1.8 | – | – | – | 12 | 12 |
| 1.8–2.0 | – | – | – | 8 | 8 |
| 2.0–2.6 | – | – | – | 6 | 6 |
| 2.6–2.8 | – | – | – | 1 | 1 |
| sum | | | | | 1346 |

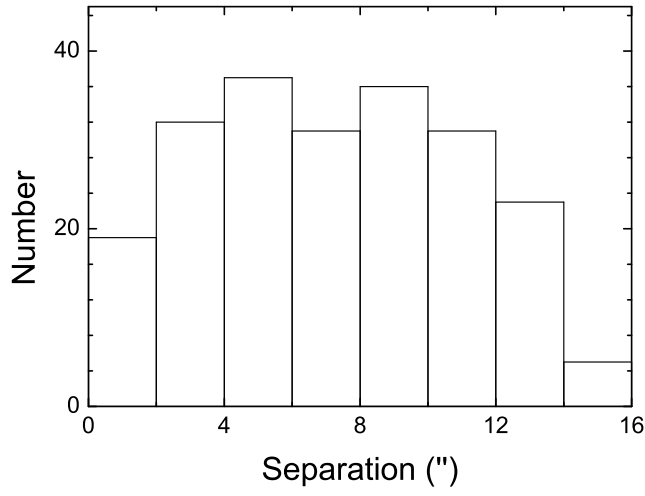


Fig. 1.— Number of sources as a function of the separations of the pair of GLIMPSE point source and GBPS source in our observing sample.

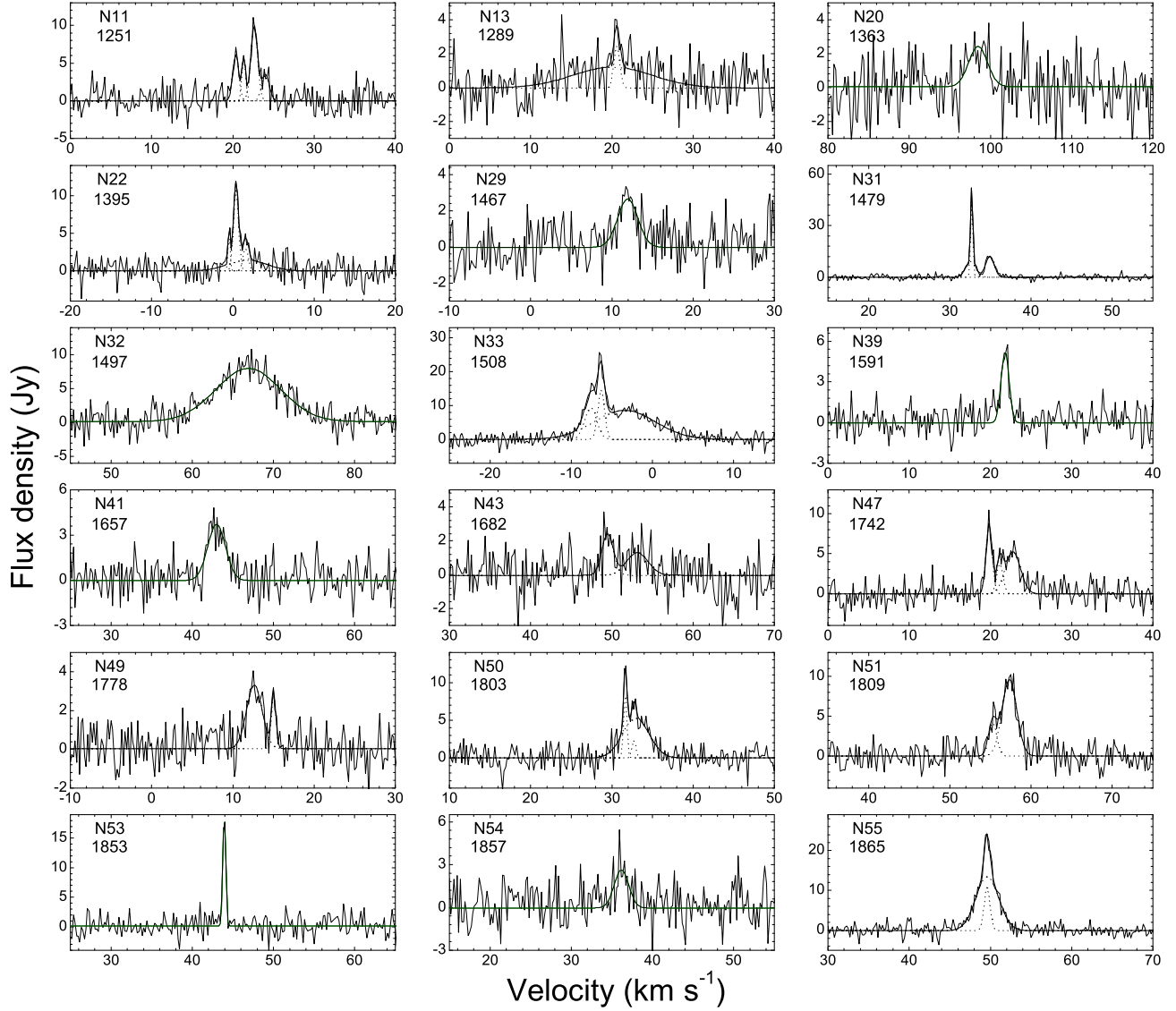


Fig. 2.— Spectra of the 95 GHz methanol masers detected in the survey. The dashed lines represent the Gaussian fitting of each maser feature, the bold-solid line mark the sum of the Gaussian fitting of all maser feature.

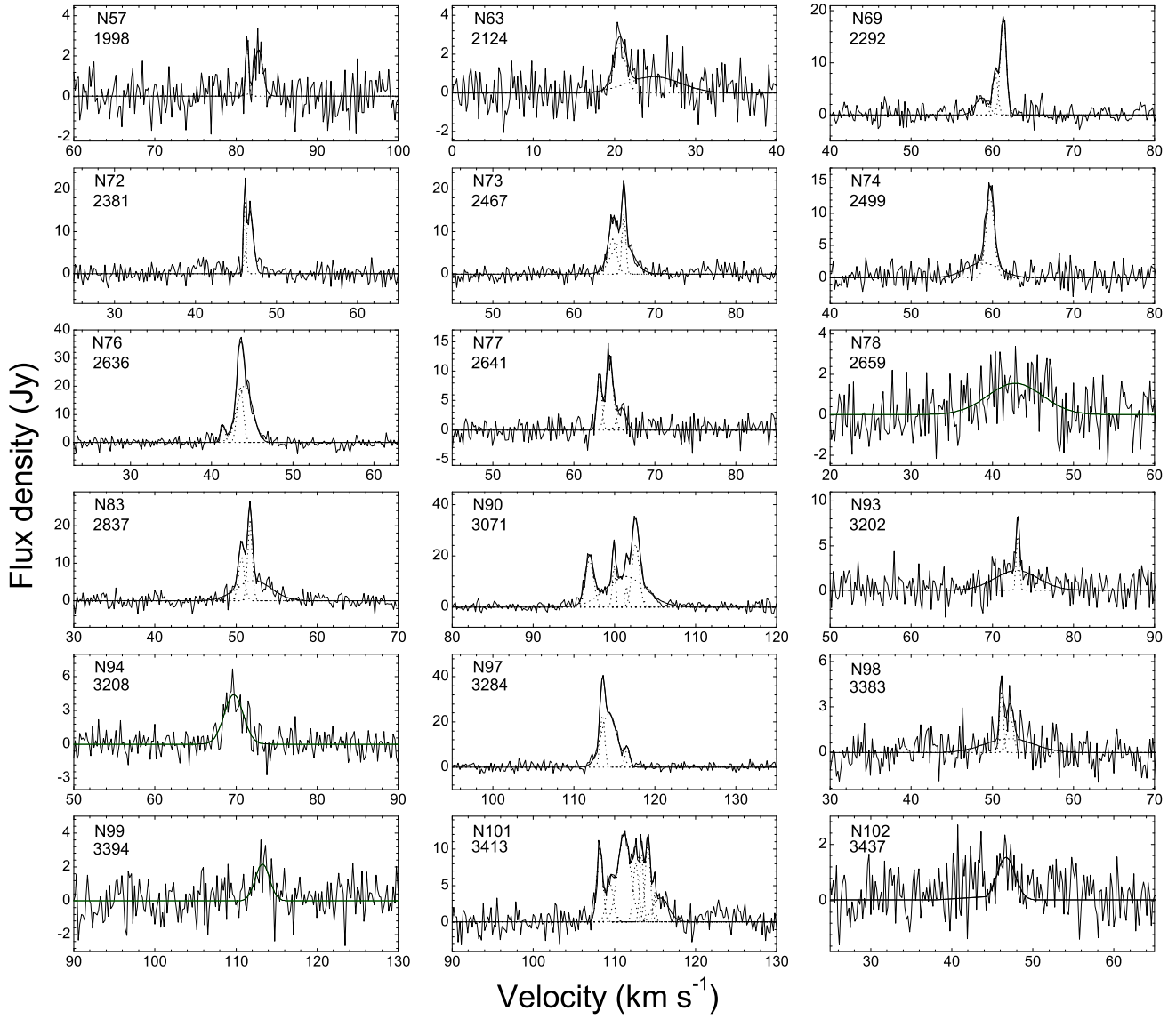


Fig. 2.— Continued.

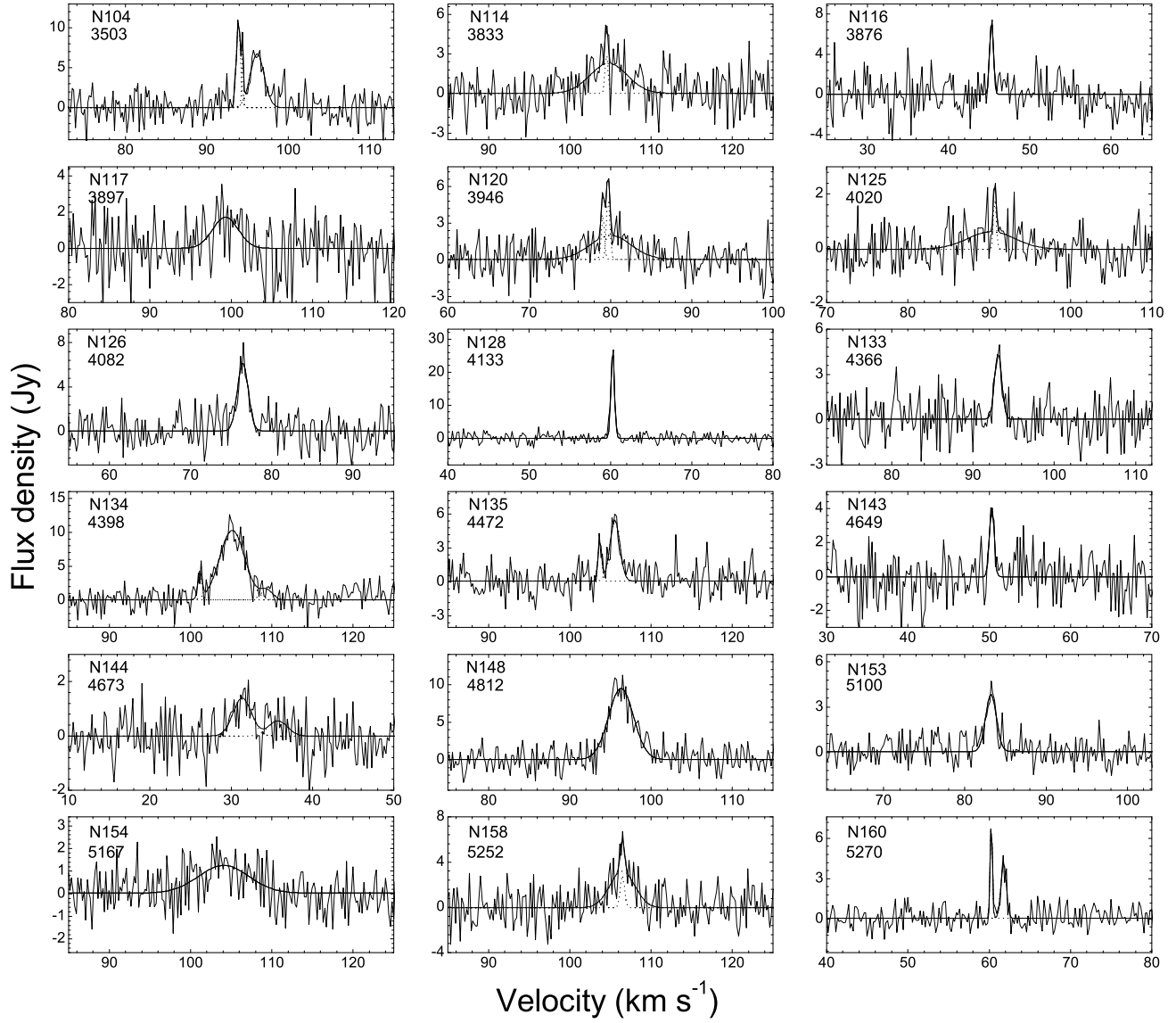


Fig. 2.— Continued.

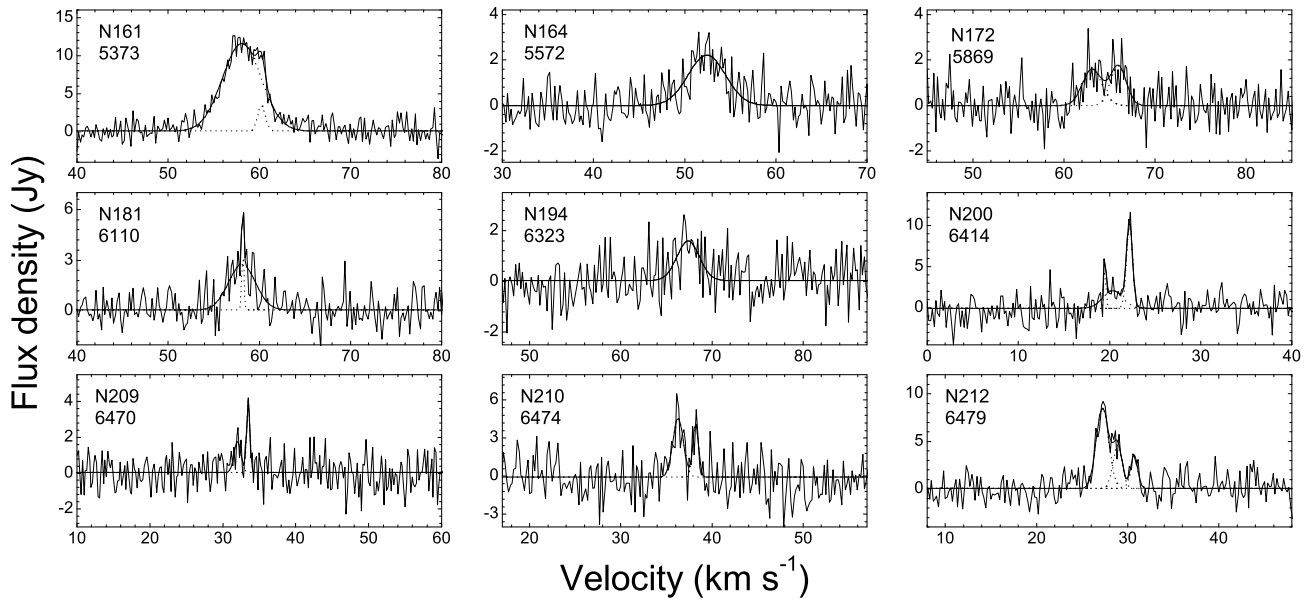


Fig. 2.— Continued.

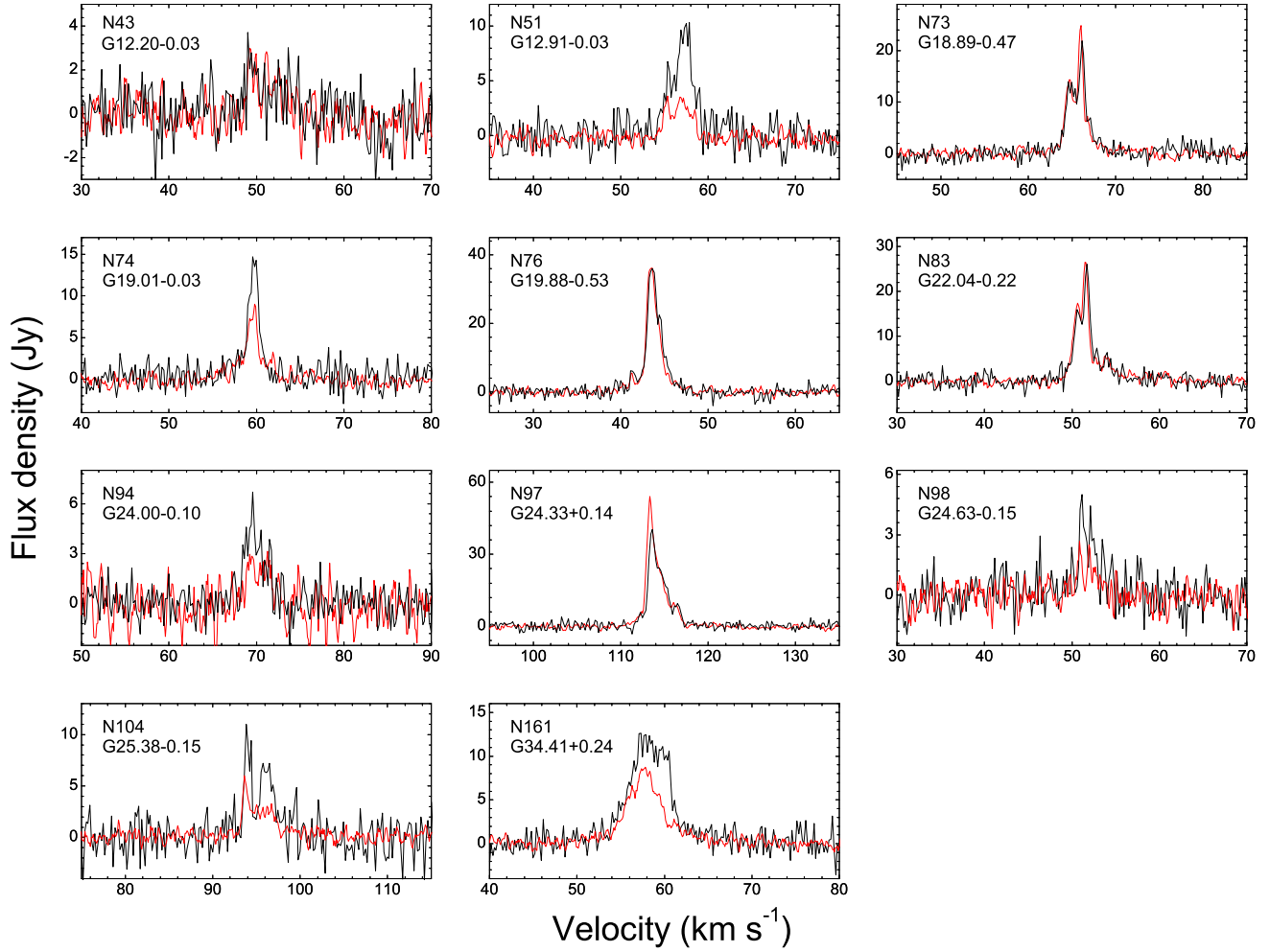


Fig. 3.— Comparison of the spectra of 95 GHz methanol maser emission in the 11 sources which have been detected in both the PMO 13.7-m survey (this work) marked with black lines and the EGO-based Mopra survey by Chen et al. (2011) marked with red lines. A color version of this figure is available in the online journal.

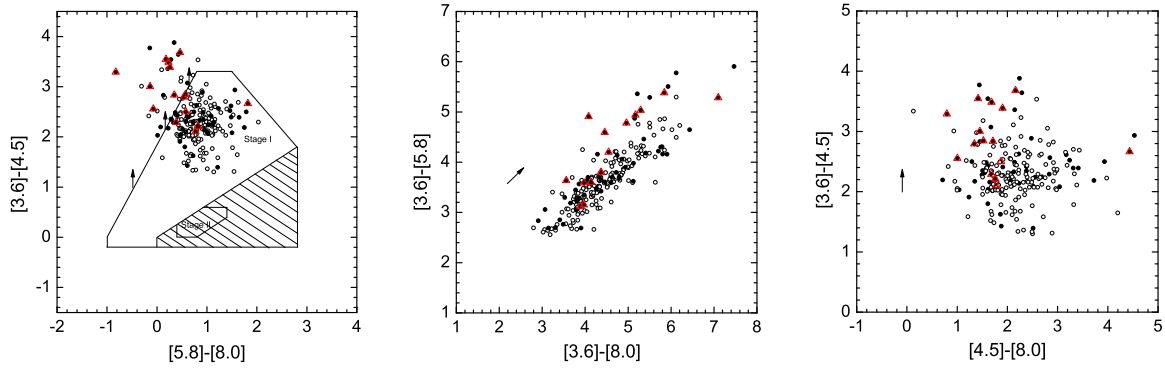


Fig. 4.— Color-color diagrams of GLIMPSE point sources associated with and without class I methanol maser detections in the survey. Filled and open circles represent the sources with and without class I methanol maser detections, respectively. The sources associated with EGOs (15 in total) are enclosed by red triangles. The solid lines overlaid in $[3.6]-[4.5]$ vs. $[5.8]-[8.0]$ diagram construct the regions occupied by various evolutionary-stage (Stages I, II and III) YSOs according to the models of Robitaille et al. (2006). The hatched region in the color-color plot is the region where models of all evolutionary stages can be present. Note that the Stage II area in the color-color plot is hatched to show that most models in this region are Stage II models, however Stage I models can also be found within this area. The reddening vectors in each panel show an extinction of $A_v=20$, assuming the Indebetouw et al. (2005) extinction law. A color version of this figure is available in the online journal.

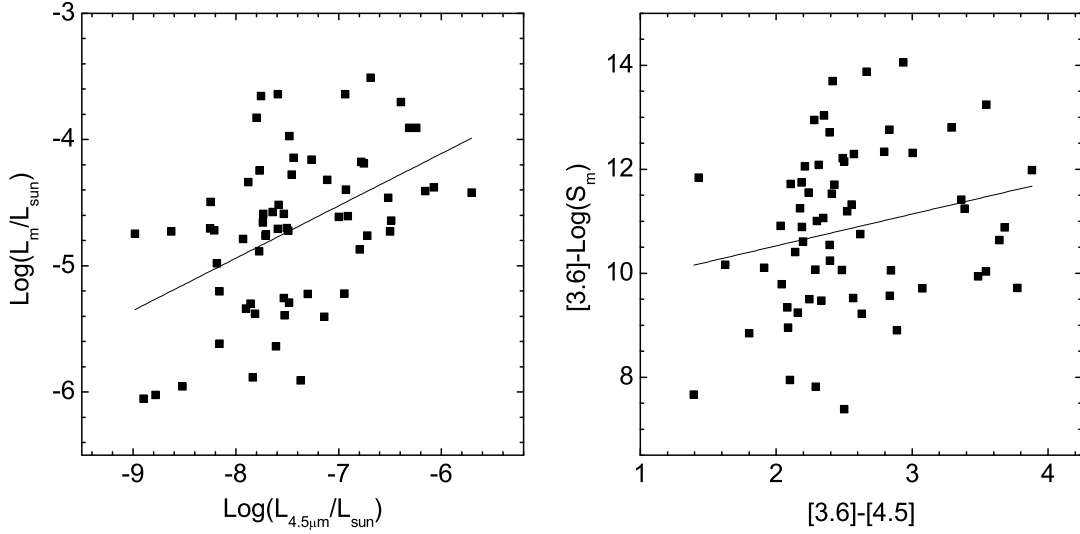


Fig. 5.— Left: logarithm of the 95 GHz class I methanol maser luminosity versus GLIMPSE point source luminosity at 4.5 μm band; Right: color-color diagram of $[3.6]-\text{log}(S_m)$ versus $[3.6]-[4.5]$ which combines the GLIMPSE point sources and class I methanol maser emission. The line in each panel marks the best fit to the corresponding distribution.

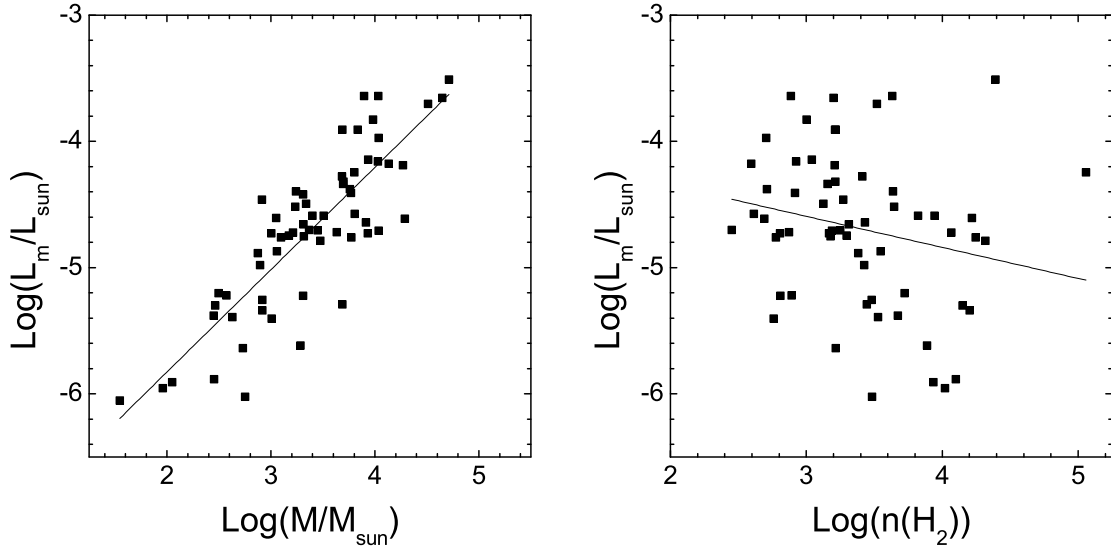


Fig. 6.— Logarithm of the 95 GHz class I methanol maser luminosity as a function of the gas mass (left panel) and H_2 volume density (right panel) of the associated 1.1 mm BGPS sources. The line in each panel marks the best fit from the linear regression analysis to the corresponding distribution.

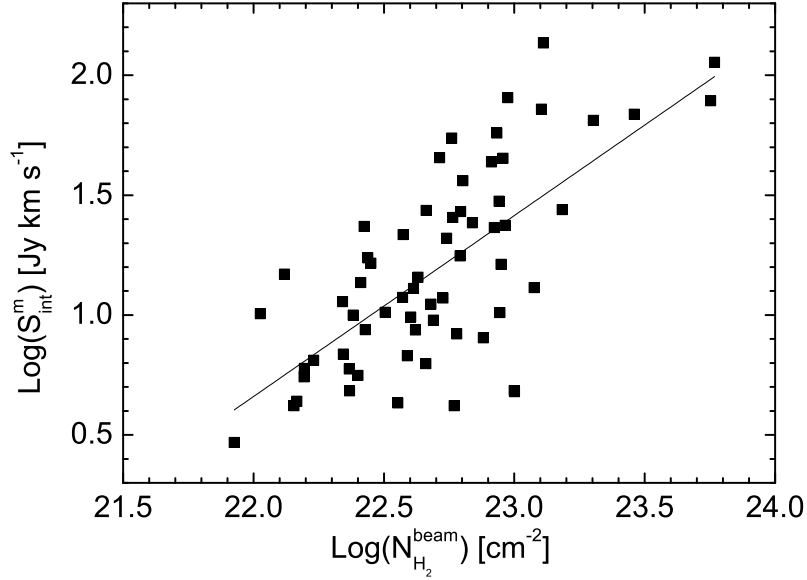


Fig. 7.— Logarithm of the integrated flux density of the 95 GHz class I methanol maser as a function of the beam-averaged H_2 column density of the BGPS source. The line marks the best fit from the linear regression analysis to the distribution.

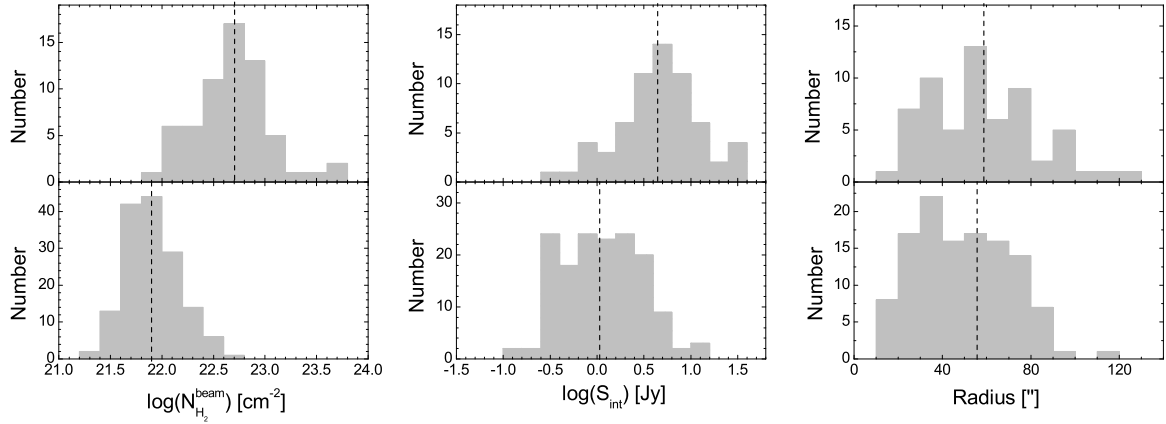


Fig. 8.— Number of sources as functions of the BGPS beam-averaged H_2 column density (left), integrated flux density of the BGPS source (middle) and BGPS source radius (right) for the two groups with and without class I methanol maser detections. For distributions in each BGPS property, the upper and lower panels correspond to the BGPS sources with and without class I methanol maser detections. The mean of each distribution is marked by the vertical dashed line in the corresponding distribution.

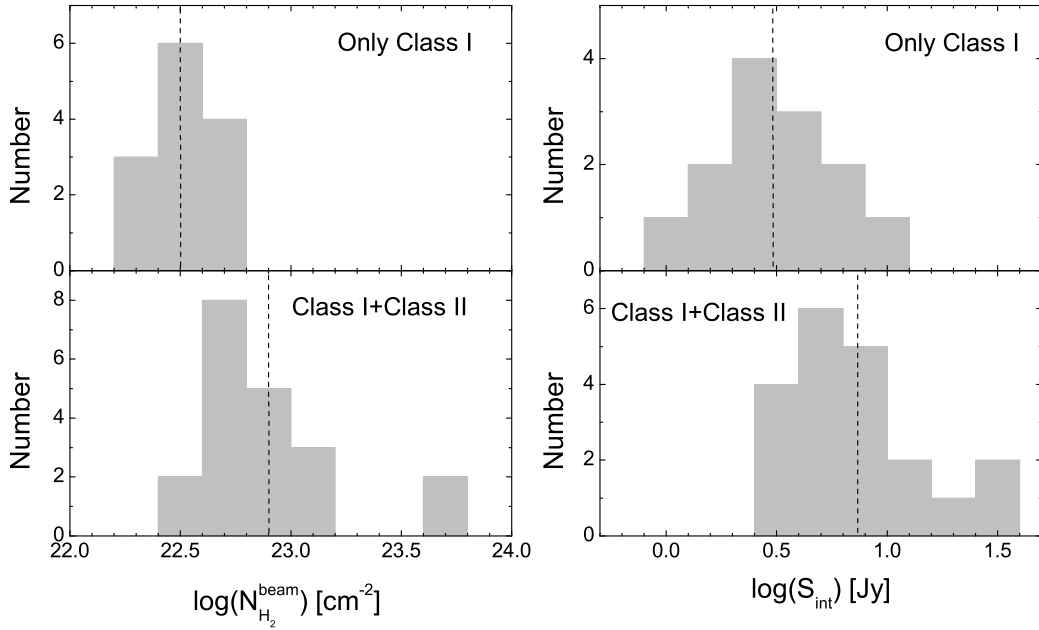


Fig. 9.— Number of sources as functions of the BGPS beam-averaged H₂ column density (left) and BGPS integrated flux density (right) for the two subsamples based on which class of methanol masers they are associated with. For distributions in each BGPS property, the upper and lower panels correspond to the BGPS sources associated with only class I methanol masers and associated with both class I and II methanol masers, respectively. The mean of each distribution is marked by the vertical dashed line in the corresponding distribution.

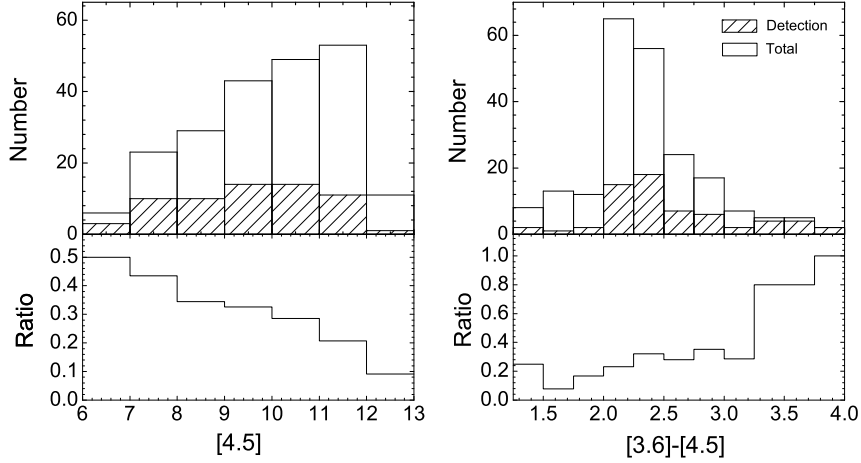


Fig. 10.— Detection rates of class I methanol masers with $4.5 \mu\text{m}$ magnitude (left panel) and $[3.6]-[4.5]$ color (right panel) of the GLIMPSE point sources. For each mid-IR property, the upper panel shows the histogram distributions of number of total sample sources and detected class I methanol maser sources marked with open bars and diagonal bars, respectively, and the lower panel shows the corresponding detection rate of class I methanol maser in each statistical bin.

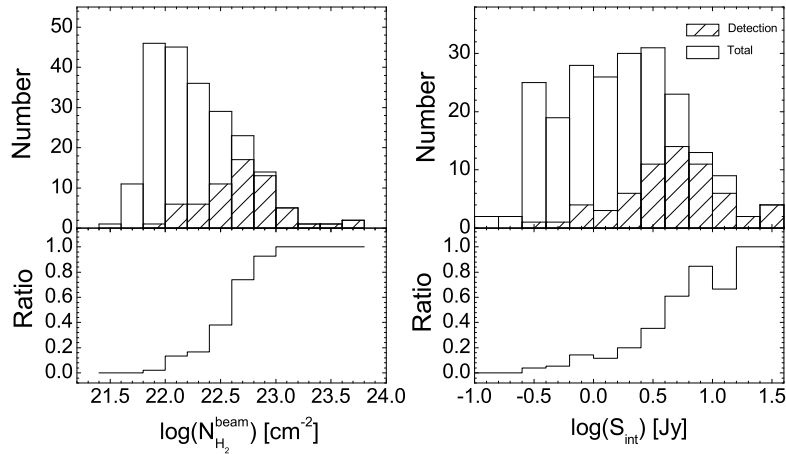


Fig. 11.— As Figure 10, but for detection rates of class I methanol maser with the BGPS properties of the beam-averaged H_2 column density (left), integrated flux density (right).

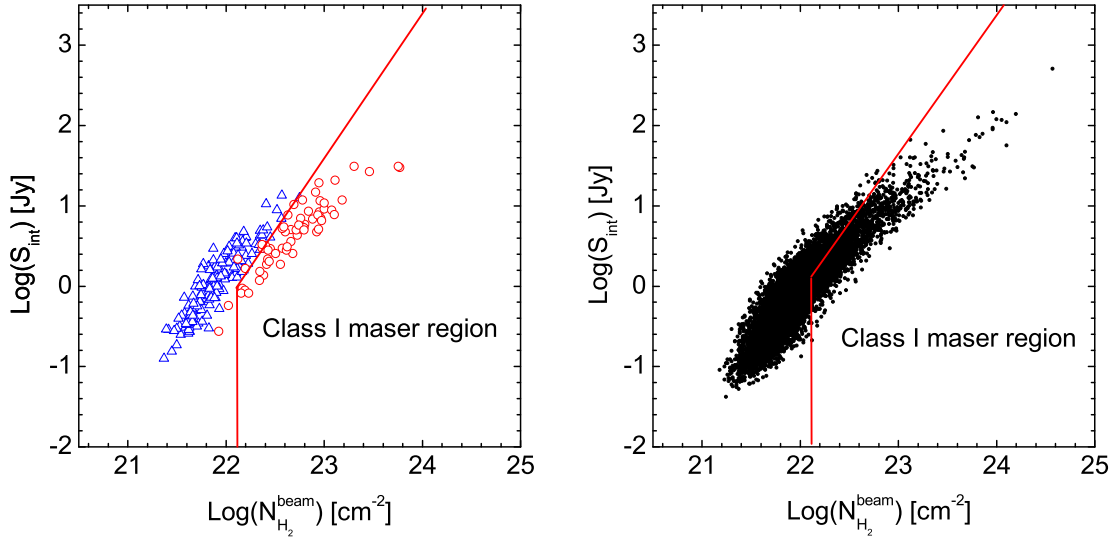


Fig. 12.— Left panel: Logarithm of the integrated flux densities versus beam-averaged H_2 column density of BGPS sources with and without class I methanol maser detections (marked by red circles and blue triangles, respectively) in our current survey sample, the class I methanol maser locating region is enclosed by the red lines. Right panel: As Left panel, but for all cataloged BGPS sources. (A color version of this figure is available in the online journal.)